GEORG-AUGUST-UNIVERSITÄT
GÖTTINGEN

Fakultät für
Physik

Master's Thesis

Ein minimales Modell für flüssig-gas Koexistenz in feuchter granularer Materie: Implementierung, Verifikation und Charakterisierung

A minimal model for liquid-gas coexistence in wet granular matter: Implementation, verification, and characterization

prepared by

Mitja Kleider

from Hannover

at the Max Planck Institute for Dynamics and Self-Organisation (MPIDS)

Thesis period:	3rd March 2012 until 1st September 2012
First referee:	apl. Prof. Dr. Jürgen Vollmer
Second referee:	Dr. Claus Heussinger

Abstract

Due to its dissipative nature, wet granular matter is a great model system for non-equilibrium thermodynamics. We propose a new thermostating scheme minimal model that injects energy into the system via collisions with non-moving walls. Using event-driven MD simulations, that were developed from scratch, we demonstrate that this driving can lead to solid-like, liquid-like and gas-like phases, and that for certain amounts of energy input this model also shows phase coexistence. The different granular phases is characterized by observing macroscopic quantities like temperature and density. With this we hence provide a minimal model system with great prospect to understand in more detail the physics of granular phase transitions.

Contents

1 Introduction

The term granular matter describes an accumulation of solid, macroscopic particles under conditions where Brownian motion of the grains is negligible. It is well known from everyday life, for example as sand, coffee beans or washing powder, which are all packed, shaken, poured and mixed in our daily routines. When doing so granulates hold a multitude of surprises: if cereal is shaken, its components do not mix. Rather the bigger flakes or nuts will move to the top. This is known as the brazil-nut effect [33]. Dense packings can also support surprising loads, for example, a pack of coffee does not deform much until the vacuum sealing is broken. In contrast to fluids, the flow rate of sand in an hourglass does not depend on the height of the sandpillar in the upper half. Flowing dry granular matter even shows the Plateau-Rayleigh instability, i.e., the breakup of a stream into drops, known from water flowing out of a tap [40].

In industrial processing granular matter also plays a major role [15]. Raw materials are often processed as grains or powder. A classical problem in pharmaceutical and chemical industry is spontaneous plugging, e.g., in air activated powder ducts [16]. Another industrial problem is jamming during discharge from a silo, where the resulting pressure at the walls can lead to the collapse of silos and hoppers.

It is now recognized that these features result from the peculiar effective interaction laws of granular particles. Usually these particles carry no electric charge. Therefore in granular matter other forces than the forces between microscopic particles become important. This is explained further in section 2.2.

Granular matter is a popular model system for the study of non-equilibrium thermodynamics, because of its strong dissipative nature. Grains dissipate kinetic energy via their internal degrees of freedom. A wealth of additional phenomena arise when granular particles also interact via adhesion, e.g., due to the presence of a fluid forming capillary bridges. We call these systems *wet granular matter*. The most popular example of wet granular matter are sandcastles. If water is added to

granular matter in the form of sand, one can build beautiful castles and sculptures (Fig. 1.1a). The water between particles forms capillary bridges, which hold the

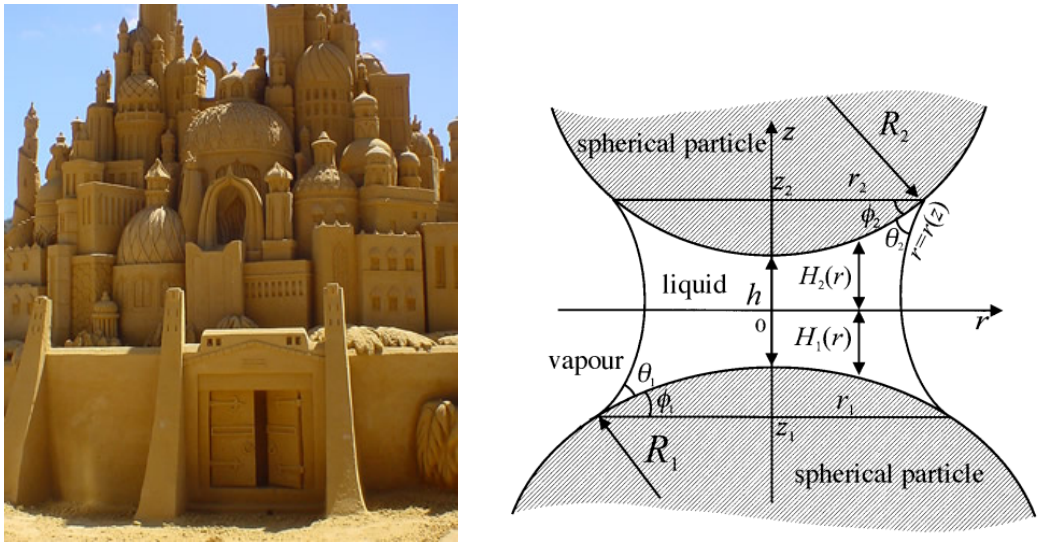

Figure 1.1: Left: A sandcastle is the most popular example for wet granular matter. Most people know from experience that dry sand is flowing through our fingers, while a sandcastle remains solid when a certain amount of water is added. Image from Wikimedia Commons. Right: Sketch of a liquid capillary bridge between two spherical particles, taken from [3].

particles together (Fig. 1.1b). The amount of water is not important, there is no recipe for sandcastles, provided there is enough to fill the surface roughness of the grains and form capillary bridges. If too much water is added, the solid structure is flowing again: The air has been replaced by water, creating a different form of dry granular matter. In view of this one understands that heavy rain can lead to land- or mudslides [12] (Fig. 1.2). Therefore the fluidization is an important subject of research [4, 38]. If the experiment needs to be conducted under water, for example with an external flow field provided by a water stream, (silicon-)oil can be used to form capillary bridges [4].

When the particles are strongly agitated – e.g., in an avalanche – capillary bridges only form upon collision, i.e., at any given time most of the particles do *not* form capillary bridges. Such granular gases can also be found in interstellar dust clouds, like in the rings of Saturn. They can also be produced in experiments, for example by shaking glass or plastic beads [48].

Figure 1.2: Example of major mudslides in Venezuela (dark brown color in the left image, light brown color in the right image). The disaster is known as the *Vargas tragedy* in December 1999, causing many deaths and extensive damage to towns, cities and infrastructure. Heavy rain triggered thousands of shallow landslides that evolved into debris flows. Images from Wikimedia Commons.

1.1 Phase Transitions

In the previous section we have seen examples where granular matter behaves like a solid, like a fluid, and like a gas. For condensed matter at thermal equilibrium, the example of collective behaviour known as *phase transitions* is well understood and considered textbook knowledge [50]. Phase transitions far from equilibrium are similar, but less well understood. Quoting Axel Fingerle [21], "well-known examples that are currently of great interest range from collective pattern formation in systems of molecular and micron scale to transitions in social behavior."

Interesting topics concerning granular matter are, for example, fluidization by vibration and phase separation [25]. Our quest is understanding the phase diagram and phase transitions of wet granular matter. The phase diagram of vertically agitated wet granular matter was determined experimentally and numerically [21], referring to an experimental setup, which is sketched in Fig. 1.3.

1.2 Numerical Simulations

With numerical simulations one can predict and optimize devices before they are built, e.g., rotating drums for industrial applications. Some simulations can replace expensive, time consuming, or dangerous experiments. Access to numerical data allows observation of some parameters with less effort. Other parameters can not

be determined experimentally at all. If one is interested in parameter ranges that are not accessible experimentally, they may be accessible in numerical simulations.

This thesis is motivated by a liquid-gas coexistence regime observed both in experiments (Fig. 1.3) and quasi-realistic numerical simulations (Fig. 4.2). In chapter 2, a short introduction to the non-equilibrium features of dry and wet granular matter is given in sections 2.1 and 2.2, respectively. The numerical methods are introduced in section 2.3. Their implementation is verified in chapter 3. Chapter 4 introduces a phase diagram (section 4.1) obtained numerically by Klaus Röller. A minimal model for a system showing phase coexistence to simplify its theoretical description is defined in section 4.2. The numerical results using this minimal model are presented in section 4.3 and discussed in chapter 5.

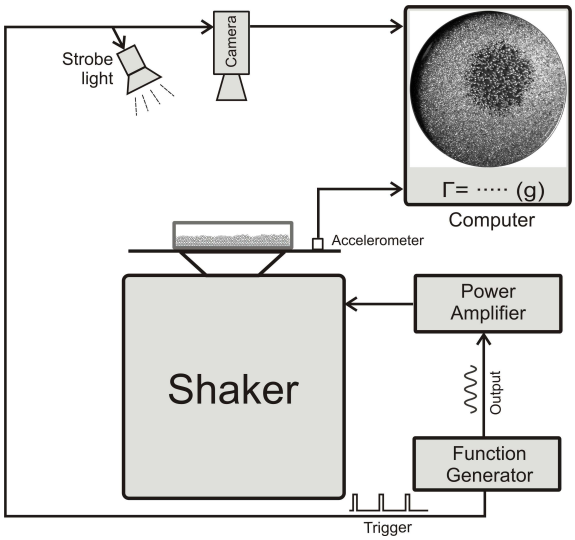

Figure 1.3: Experimental setup [28]. A wide and flat cylindrical petri dish (diameter 14cm) is shaken vertically. It is filled about two-thirds of its height by spherical glass beads with average diameter in the order of 1mm, i.e., $6-7$ layers at rest. The glass beads are wetted by water or nonane. Shaking with amplitude A and angular frequency ω is performed by an electromagnetic shaker driven by a function generator. The resulting time-dependent height of the ground plate relative to its average position is $z(t) = A\cos(\omega t)$. The signal also triggers a strobe light illuminating the petri dish from above. This ensures that all images are taken at the same height $z(t)$. The dimensionless control parameter *peak acceleration* Γ (see section 2.1) can be compared with the acceleration measured by an accelerometer. An example image is depicted at the upper right corner. Glass spheres appear as bright dots on the dark background. Thus areas with low density look darker than areas with high density. In the example image you can observe a gas bubble inside a condensed fluid phase.

2 Theory and Numerical Implementation

In an effective microscopic description the particle interaction can be modeled by an elastic interaction force [26] and for macroscopic particles there can be also additional dissipative force [9] as further specified in section 2.2. The motion of particles is given by Newton's equations of motion:

$$m_i \frac{d^2\mathbf{r}_i}{dt^2} = \mathbf{F}_i(\mathbf{r}_1, \mathbf{v}_1, \mathbf{r}_2, \mathbf{v}_2, \ldots, \mathbf{r}_N, \mathbf{v}_N) \tag{2.1}$$

These equations can be numerically integrated to determine the particle trajectories in molecular dynamics simulations (section 2.3.1).

Granular gases may be described by varying amounts of detail. Instead of describing the granular gas by positions $\mathbf{r}_i$ and velocities $\mathbf{v}_i$ of particles, it may also be described by hydrodynamic equations for its coarse-grained properties number density $n(\mathbf{r}, t)$, flow velocity $u(\mathbf{r}, t)$, and temperature $T(\mathbf{r}, t)$. Their gradients induce macroscopic flows of mass, momentum and energy [8].

2.1 Dissipation and Energy Input

In granular matter energy is dissipated due to collisions. The ratio between initial relative velocity v_{initial} in radial direction, i.e., the direction of the distance vector between two colliding particles, and the final velocity v_{final} after a the collision is called coefficient of restitution ε. It is frequently assumed to be a material constant in the form of

$$\varepsilon = \frac{v_{\text{final}}}{v_{\text{initial}}}. \tag{2.2}$$

This relates initial and final kinetic energy as

$$E_{\text{final}} = \varepsilon^2 E_{\text{initial}}. \tag{2.3}$$

The dissipated energy is transferred to the grains' internal degrees of freedom like deformation and heat. Compared to the kinetic energy of a particle, the resulting increase of temperature is negligible. Owing to its highly dissipative nature, granular matter is a great model system for non-equilibrium thermodynamics.

A granular system with dissipation and no energy input will undergo free cooling. Kinetic energy is dissipated until no particle is moving. A detailed account of studies on free cooling of dry granular matter can be found in [8].

To maintain motion of particles additional energy needs to be supplied. Kinetic energy can be injected into the system by external driving, like shaking, tapping and shearing. One of the most convenient ways to inject energy in experiments is vertical shaking (see Fig. 1.3 for an illustration). For a vibrated system under gravity g the most important control parameter (see section 4.1) is the ratio of maximum acceleration of the moving ground plate and the gravitational acceleration [41]. This parameter, Γ, is called peak acceleration. For sinusoidal shaking, $z(t) = A\cos(\omega t)$, it amounts to

$$\Gamma = \frac{A\omega^2}{g}, \tag{2.4}$$

where A and ω are the amplitude and angular frequency of the vibration, respectively.

Low values of Γ allow the system to approach a non-zero temperature by moving towards a configuration of lower potential energy and increasing packing fraction. When the vibrational acceleration is larger than the one due to gravitation ($\Gamma > 1$), several types of symmetry-breaking instabilities can occur. Faraday reported his observation of convection in vibrated granular matter in 1831. Higher values of Γ show standing waves in two dimensions [11, 13] or patterns in three dimensions [6, 32]. For sufficiently large Γ the system shows a fluid state [18, 35]. Due to its dissipative nature, the system shows an instability that forms coherently moving clusters [22]. The theoretical consequences are described in [14, 52].

Some thermodynamic principles can be applied to granular matter. Consider a homogeneous and isotropic granular gas of infinite extension in the absence of external forces. Analogously to molecular gases, the random motions can be regarded as a *granular temperature*. It depends on the particle velocities via $T_g \propto \langle v^2\rangle - \langle v\rangle^2$. Assuming the average velocity to be zero, we define the granular temperature of a

system of N particles with velocities $\mathbf{v}_i$, $i = 1 \dots N$, as

$$T_g = \frac{2}{f_d} \frac{1}{N} \sum_{i=1}^{N} \frac{m_i \mathbf{v}_i^2}{2}, \tag{2.5}$$

where f_d are the translational degrees of freedom. In the spirit of kinetic theory one can also define pressure, particle diffusion, and transport of momentum and energy. A full analogy to ordinary thermodynamics cannot be achieved. Our hope is that this work will contribute to a better understanding of the relation between these quantities.

2.2 Wet Granular Matter

Here, different effective microscopic descriptions of wet granular matter are introduced. For simplicity, molecular degrees of freedom inside a particle are neglected and replaced by a model accounting for the forces which occur due to molecular interaction. Particles of irregular shape can be approximated by an accumulation of spherical particles [5, 41]. Different approaches modeling normal and tangential forces between colliding spherical particles have been proposed, e.g., the hard core interaction model, linear dashpot model, Hertz model and Walton and Braun's model [36, 53, 54]. There is usually a component of repulsion because of elastic deformation and a component responsible for the dissipative energy loss.

Between granular particles which are not in contact, several other – mostly cohesive – forces can act, like van der Waals forces, electrostatic forces, gravitational forces, or capillary bridge forces. Their magnitude as a function of particle diameter is shown in Fig. 2.1. The capillary bridge force results from the surface tension and resulting Laplace pressure between the wetting liquid (e.g., water) and the surrounding atmosphere (e.g., air). See [43] for experimental details. For granular particles it is the strongest inter-particle force and therefore has the most significant influence on the physical behaviour of granular matter. The past focus of research was mainly on dry granular matter or powders. Still there is a decent amount of work dedicated to wet granular matter (see for example [7, 25, 27, 34, 42] and references therein).

A capillary bridge is formed when two particles, wetted by a liquid film, touch (sketched in Fig. 2.2). This liquid bridge gives rise to an adhesive force and – under dynamic conditions – an additional force due to viscous dissipation [29]. At a critical separation s_{crit} the capillary bridge will rupture and only reform when the particles

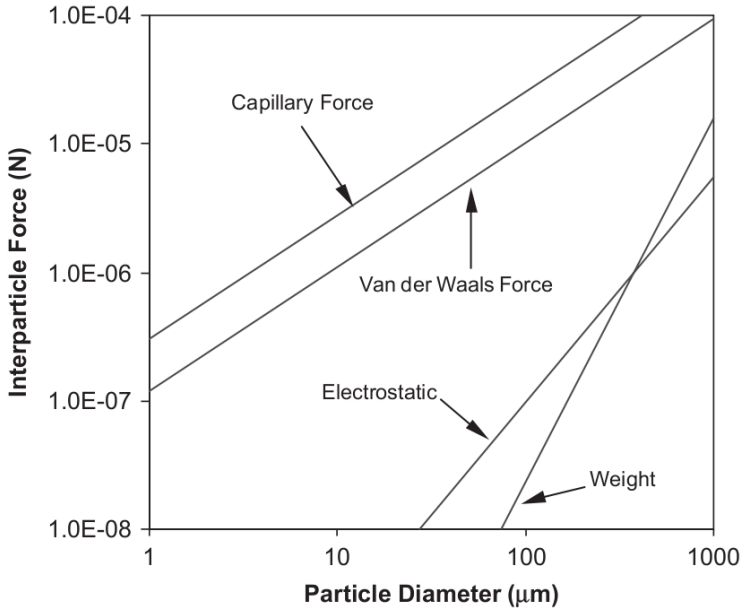

Figure 2.1: Interparticle force in dependence of particle diameter. [54]

touch again. Thus the formation and rupture is a hysteretic process which dissipates energy. The total amount of energy dissipated during separation and by rupture will be called capillary bridge energy E_{cb} henceforth.

2.2.1 Capillary Bridge Models

The capillary bridge force has been determined experimentally (Fig. 2.3). However, many physical aspects in the liquid and gas phase of the system do not depend on the detailed functional form of the underlying force [41]. Consequently, simpler models can be used in numerical simulations. The *minimal capillary model* [25] (Fig. 2.4a) assumes a constant force, F_B, independent of separation until rupture at a critical separation, s_{crit}. The dissipated capillary bridge energy is $E_{cb} = F_B \cdot s_{\mathrm{crit}}$. In some cases only the capillary bridge energy E_{cb} is important [41]. This inspired the *thin-thread model* [21], which assumes that no force is acting until the particles are at critical separation s_{crit}. The capillary bridge force is modeled as delta distribution $F = E_{cb} \cdot \delta(s - s_{\mathrm{crit}})$ such that the area under the distribution again gives E_{cb} (Fig. 2.4b).

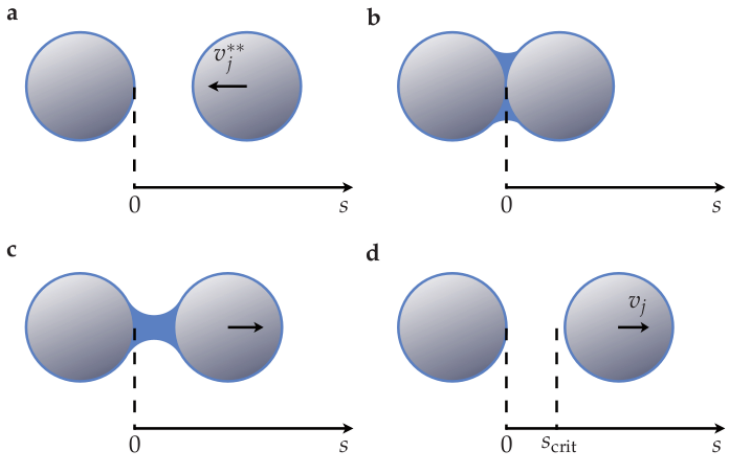

Figure 2.2: Formation and rupture of a capillary bridge [41]. Two wetted particles approach each other (a). When they collide, a capillary bridge is formed (b) which exerts force (c) until rupture at the critical separation s_{crit} (d).

2.3 Molecular Dynamics Methods

A molecular dynamics (MD) method is the process of generating trajectories of a system containing N particles subject to an interparticle potential and reasonable initial and boundary conditions. Trajectories are obtained by direct numerical integration of Newton's equations of motion.

For comparison of the experimental setup described in section 1.1 with numerical results, Klaus Röller took the effort to model sinusoidally moving walls in a system under gravity and matched the numerical system parameters to the experimental setup [41]. Some of his findings are discussed in section 4.1. As it is hard to find a theoretical description under such conditions, in this thesis we are looking for a simplified minimal model which shows similar behaviour.

2.3.1 Time-Driven MD

For spherical particles the dynamics of granular matter is governed by Newton's equations of motion for the center of mass coordinates of its particles i ($i = 1, \ldots, N$)

$$\frac{\partial^2 \boldsymbol{r}_i}{\partial t^2} = \frac{1}{m_i} \boldsymbol{F}_i(\{\boldsymbol{r}_j, \boldsymbol{v}_j, \boldsymbol{\varphi}_j, \boldsymbol{\omega}_j\}) \tag{2.6}$$

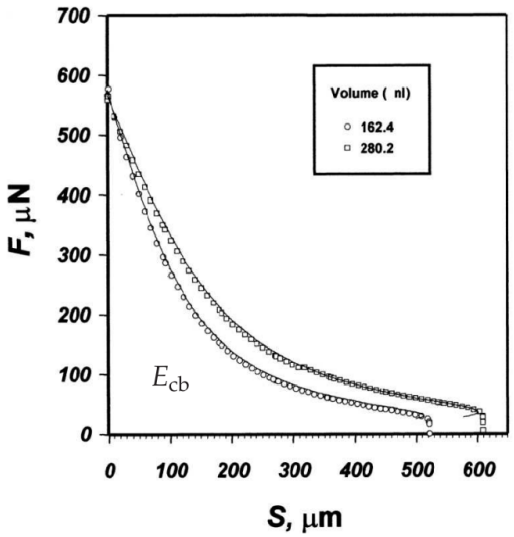

Figure 2.3: Capillary bridge force F between a spherical particle and a flat wall in dependence of surface separation s [49]. Circles and squares denote experimental results for different liquid volumes, straight lines show the solution of the Young-Laplace equation. The shape of the capillary bridge force between two spherical particles is similar [37].

and for the respective Euler angles

$$\frac{\partial^2 \boldsymbol{\varphi}_i}{\partial t^2} = \frac{1}{\hat{J}_i} \boldsymbol{M}_i(\{\boldsymbol{r}_j, \boldsymbol{v}_j, \boldsymbol{\varphi}_j, \boldsymbol{\omega}_j\}), \tag{2.7}$$

where $j = 1, \ldots, N$. The force $\boldsymbol{F}_i$ and torque $\boldsymbol{M}_i$, acting on particle i with mass m_i and moment of inertia $\hat{J}_i$, depend on the particle positions $\boldsymbol{r}_j$, angular orientiations $\boldsymbol{\varphi}_j$ and their corresponding velocities $\boldsymbol{v}_j$ and $\boldsymbol{\omega}_j$ of all particles $j = 1, \ldots, N$ [36]. This system of coupled differential equations is nonlinear due to appearances of the interaction forces $\boldsymbol{F}_i$ and torques $\boldsymbol{M}_i$. Hence, it can not be solved analytically. The numerical computation of trajectories of all particles is an approximate solution, known as (force-based) *Molecular Dynamics* [1], which is described in standard textbooks on modern Molecular Dynamics such as [2].

Central to this method is the computation of the forces and torques. Considering only short-range forces, i.e., via mechanical contact, the force $\boldsymbol{F}_i$ and torque $\boldsymbol{M}_i$ acting upon a particle i are given by summation of the pairwise interaction $\boldsymbol{F}_{ij}$,

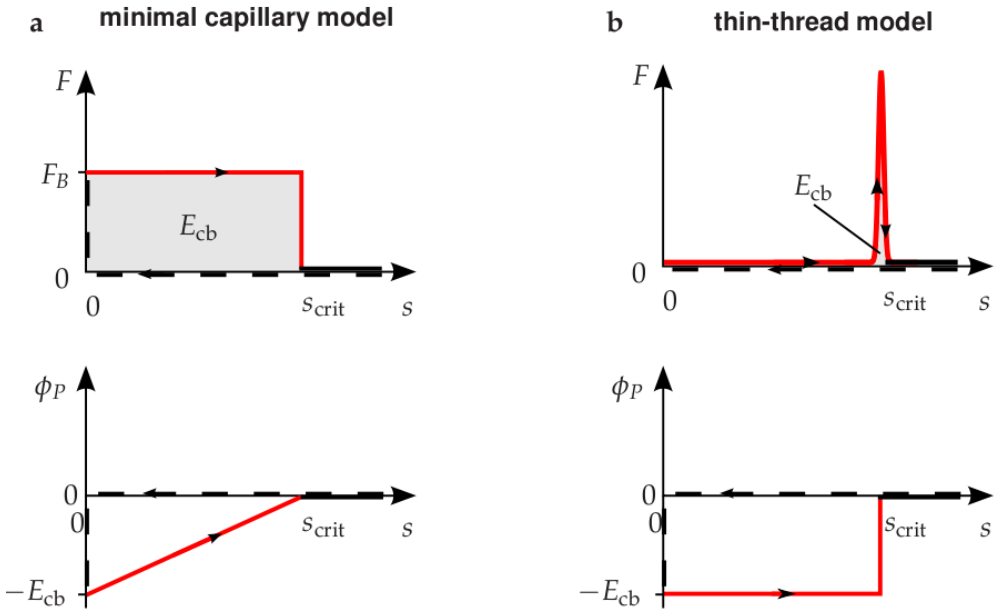

Figure 2.4: Capillary bridge models [41]. In both models there is no capillary bridge force acting until the particles touch (dashed black line). In the minimal capillary model (a) the force has a constant value F_B until the bridge ruptures. The performed work is $E_{cb} = F_B \cdot s_{\text{crit}}$. In a pseudo-potential representation this model jumps to $-E_{cb}$ at collision and goes back to zero potential at s_{crit} with a constant slope. The thin-thread model (b) has a different approach: no force is acting after collision until the particles are at critical separation s_{crit}. There is a force peak at s_{crit} with area E_{cb}. This model looks like a hysteretic square-well potential in pseudo-potential representation.

$\boldsymbol{M}_{ij}$ of the particle with all other particles of the system:

$$\boldsymbol{F}_i = \sum_{j=1, j\neq i}^{N} \boldsymbol{F}_{ij}, \tag{2.8}$$

$$\boldsymbol{M}_i = \sum_{j=1, j\neq i}^{N} \boldsymbol{M}_{ij}. \tag{2.9}$$

The interaction laws for the pairwise forces $\boldsymbol{F}_{ij}$ and torques $\boldsymbol{M}_{ij}$ are model specific.

We will summarize one model used for the simulation of spherical granular particles in [41], because some of the results are presented in section 4.1. The torque and forces tangential to the particle surface were neglected. For the normal force

component, the following modified version of the Hertz model (see [36, p. 21]) was used:

$$F(\zeta) = \frac{2Y\sqrt{R_{\text{eff}}}}{3(1-\nu_p^2)}\left(\zeta^{\frac{3}{2}} + A_d\sqrt{\zeta}\frac{\mathrm{d}\zeta}{\mathrm{d}t}\right), \tag{2.10}$$

with effective radius $\frac{1}{R_{\text{eff}}} = \frac{1}{R_i} + \frac{1}{R_j}$ of the spheres i and j with radii R_i and R_j, deformation $\zeta = R_i + R_j - |\boldsymbol{r}_i - \boldsymbol{r}_j|$ and the material parameters Young modulus Y, Poisson ratio ν_p and dissipative constant A_d. The Gear integration scheme has proven to be successful as time-driven integration method for granular matter [36, p. 26] and was also employed in [41]. The force-based model for capillary bridge interaction is the minimal capillary model introduced in section 2.2.1.

In this thesis we are using a different approach which was also used in [41], and is presented below.

2.3.2 Event-Driven MD

If the typical duration of a collision is much shorter than the mean time between collisions, particles are very rarely in contact with more than one other particle. As collisions are of very short duration, the particles propagate along ballistic trajectories most of the time. For such systems, e.g., granular gases, one may assume that the statistical properties of the system are determined by pairwise (also known as binary) and instantaneous collisions [8]. This assumption is also called hard-particle approximation. In strict mathematical sense multi-body collisions can be excluded only for an infinitely steep interaction potential or for vanishing particle density [8], but still these models provide valuable insight into the properties of real gases also far beyond this regime (see e.g., [1, 2, 39]).

If there are only binary, instantaneous collisions, force-based molecular dynamics is applicable, but the computation is very inefficient as particles are mostly propagating without interaction. A more efficient approach in this case is straight-forward analytical integration, which tracks and takes into account the sequence of binary collision events. The positions of all particles at the time of the next collision can be calculated as they move along ballistic trajectories. The post-collision velocities can be written as functions of the pre-collision velocities. This algorithm is known as *event-driven* molecular dynamics. The computational effort only depends on the collisions, no time is spent on computations of positions and velocities between collisions. For dry granular matter the particle interaction is modeled using the coefficient of restitution introduced in section 2.1, which can be determined

experimentally or analytically from (2.10).

For wet granulates I will adopt the hard-sphere model for granular particles and the thin-thread model, which was introduced in section 2.2.1, for capillary bridges. Also in this situation the equations of motion can be solved analytically between collision events.

The so-called *collision rule*, a set of functions for the post-collision velocities will be derived in the following. In doing so we will disregard particle rotation, i.e., we assume that translational and rotational motion are not coupled. The relative velocity of colliding particles i and j at the point of contact is defined as

$$\boldsymbol{v}_{ij} = \boldsymbol{v}_i - \boldsymbol{v}_j \tag{2.11}$$

and, analogously, the post-collision velocity is denoted by the primed symbol:

$$\boldsymbol{v}'_{ij} = \boldsymbol{v}'_i - \boldsymbol{v}'_j. \tag{2.12}$$

The normal and tangential velocities are given by projections using the unit vector $\boldsymbol{e}^{\mathrm{n}}_{ij}$ pointing from particle j to particle i:

$$\boldsymbol{v}^{\mathrm{n}}_{ij} = (\boldsymbol{v}_{ij} \cdot \boldsymbol{e}^{\mathrm{n}}_{ij})\boldsymbol{e}^{\mathrm{n}}_{ij}, \tag{2.13}$$

$$\boldsymbol{v}^{\mathrm{t}}_{ij} = -\boldsymbol{e}^{\mathrm{n}}_{ij} \times (\boldsymbol{e}^{\mathrm{n}}_{ij} \times \boldsymbol{v}_{ij}). \tag{2.14}$$

The coefficient of restitution in normal direction ε is defined as

$$(\boldsymbol{v}^{\mathrm{n}}_{ij})' = -\varepsilon \boldsymbol{v}^{\mathrm{n}}_{ij}, \tag{2.15}$$

with $0 \leq \varepsilon \leq 1$. For simplicity we consider the case where all particles have the same radius R and mass $m = 1$. Conservation of linear momentum yields

$$\boldsymbol{v}'_i + \boldsymbol{v}'_j = \boldsymbol{v}_i + \boldsymbol{v}_j. \tag{2.16}$$

The post-collision velocities can be expressed as functions of the pre-collision velocities and $\boldsymbol{v}'_{ij} - \boldsymbol{v}_{ij}$ using (2.12) and (2.16):

$$\begin{aligned} 2\boldsymbol{v}'_i &= 2\boldsymbol{v}_i + \boldsymbol{v}'_{ij} - \boldsymbol{v}_{ij}, \\ 2\boldsymbol{v}'_j &= 2\boldsymbol{v}_j - \boldsymbol{v}'_{ij} + \boldsymbol{v}_{ij}. \end{aligned} \tag{2.17}$$

Moreover, using the definition (2.15), we can express $\boldsymbol{v}'_{ij} - \boldsymbol{v}_{ij}$ as

$$\boldsymbol{v}'_{ij} - \boldsymbol{v}_{ij} = -(1+\varepsilon)\boldsymbol{v}^{\mathrm{n}}_{ij}, \tag{2.18}$$

if $\boldsymbol{v}^{\mathrm{t}}_{ij}$ is preserved. Hence, combining (2.18) and (2.17) we obtain the collision rule:

$$\begin{aligned} \boldsymbol{v}'_i &= \boldsymbol{v}_i - \frac{1+\varepsilon}{2}\boldsymbol{v}^{\mathrm{n}}_{ij}, \\ \boldsymbol{v}'_j &= \boldsymbol{v}_j + \frac{1+\varepsilon}{2}\boldsymbol{v}^{\mathrm{n}}_{ij}. \end{aligned} \tag{2.19}$$

An event-driven algorithm can be sketched as follows:

1. At time $t = 0$ initialize the positions $\boldsymbol{r}_i$ and velocities $\boldsymbol{v}_i$ of all N particles. Usually it is made sure that the initial system has no center of mass velocity $\sum_{i=1}^{n} \boldsymbol{v}_i = 0$, and particles do not overlap.

2. Determine the time $t^* > t$ of the next collision event, i.e.,

$$t^* = \min(t_{ij} > t : |\boldsymbol{r}_i(t_{ij}) - \boldsymbol{r}_j(t_{ij})| = 2R,\ i, j = 1, \ldots, N) \tag{2.20}$$

3. Determine the positions of all particles at t^*. In the case without external acceleration the positions are given by

$$\boldsymbol{r}_i(t^*) = \boldsymbol{r}_i(t) + (t^* - t)\boldsymbol{v}_i \tag{2.21}$$

4. Computation of the post-collisional velocities of the two colliding particles according to (2.19).

5. Set the system time t to t^* and repeat from step 2.

In addition to particle-particle collisions, there can also be collision of a particle with a reflecting wall. In that case its velocity normal to the wall is reflected, while again the tangential component remains unchanged:

$$\boldsymbol{v}^{\mathrm{n}\prime}_i = -\varepsilon_{\mathrm{wall}}\boldsymbol{v}^{\mathrm{n}}_i. \tag{2.22}$$

Here $\varepsilon_{\mathrm{wall}}$ is the coefficient of restitution of the wall, which may be different from ε, depending on the material properties of the wall.

2.3.3 Heated Walls

The energy input introduced in section 2.1 is supplied through the boundaries in many applications. Driving by a vibrating wall with high frequency may be modeled by a *heated wall* [36]. One approach is resetting the velocity of a particle touching the wall to a value chosen from a Maxwell distribution according to a given temperature T_g. The probability distribution functions for normal and tangential velocity components can be found in [36, p. 175]. The disadvantage of this approach is that the wall temperature would not reflect, in general, the natural granular temperature in a phase-separated system, where T_g is different in the coexisting phases.

We decided therefore to use a different approach, which does not enforce a Maxwell distribution, but depends on the actual velocity of the particle and seems to be closer to the realistic shaking model used in [41]. The normal velocity component of the particle is reflected as in (2.22) with $\varepsilon_{\text{wall}} = 1$ and gets an additional term modeled after a sinusoidally moving wall:

$$v^{\text{n}\prime} = -v^{\text{n}} + 2\sqrt{\frac{E_{\text{wall}}}{m}}\cos(\xi). \tag{2.23}$$

The parameter $\xi \in [0, 2\pi]$ is a uniformly distributed random number. This additional term may result in a post-collision velocity with a direction still pointing towards the wall. If a sinusoidally moving wall was moving away from a particle because its velocity was higher than the particle velocity, there would be no collision at this time. The collision would happen later, when the wall velocity decreases or changes sign. As the heated wall is not moving, the subsequent collision rather happens instantaneously. Thus, in our wall model we chose to repeatedly reapply (2.23) with a new random number ξ until the particle is moving away from the wall, i.e., $\text{sign}(v^{\text{n}\prime}) = -\text{sign}(v^{\text{n}})$.

The amplitude of the additional term in (2.23) was chosen such that the average

energy input is E_{wall}:

$$\begin{aligned}
\langle \Delta E \rangle &= \frac{m}{2}\left\langle (v^{\text{n}\prime})^2 \right\rangle - \frac{m}{2}\left\langle (v^{\text{n}})^2 \right\rangle && (2.24)\\
&= \frac{m}{2}\left\langle (v^{\text{n}})^2 - 4\sqrt{\frac{E_{\text{wall}}}{m}}\cos(\xi)v^{\text{n}} + 4\frac{E_{\text{wall}}}{m}\cos^2(\xi)\right\rangle - \frac{m}{2}\left\langle (v^{\text{n}})^2 \right\rangle \\
&= -2m\sqrt{\frac{E_{\text{wall}}}{m}}\underbrace{\langle\cos(\xi)\rangle}_{=0} v^{\text{n}} + 2E_{\text{wall}}\underbrace{\left\langle\cos^2(\xi)\right\rangle}_{=\frac{1}{2}} \\
&= E_{\text{wall}} && (2.25)
\end{aligned}$$

2.3.4 Bridge Rupture

The formation of a capillary bridge (Fig. 2.2 between particles i and j happens at each collision event. Using the thin-thread model (Fig. 2.4b), this introduces another event involving the particles. At the time

$$t_{ij} > t : |\boldsymbol{r}_i(t_{ij}) - \boldsymbol{r}_j(t_{ij})| = 2R + s_{\text{crit}}, \tag{2.26}$$

where the surfaces of the two particles are separated by the critical rupture separation s_{crit}, the capillary bridge might rupture and dissipate the energy E_{cb} from the relative velocity between the particles in radial direction. If the kinetic energy in radial direction is not high enough, the particles will reflect at the square well potential (Fig. 2.4b) without losing energy and the capillary bridge will not rupture.

3 Verification

The implementation of the event-driven algorithm for wet granular matter is tested by comparison to the theoretical prediction for the free cooling behaviour of the numerical simulations.

3.1 Free Cooling

The driving method known as *free cooling* is mainly used in simulations and theoretical approaches [8]. Driving is reflected only in the initial conditions of the system, usually meaning random motion at the beginning which slows down over time because of dissipation in the absence of external forces. For dry granular matter, this is well studied [8, 22]. It is not easy to perform in experiments, because there are no gravitational forces. Still there is an experimental investigation for free cooling of a quasi two-dimensional granular gas [31]. For wet granular matter there are studies in one dimension [19, 51] and three dimensions [46, 47].

Let us make an estimate for the decay of granular temperature T_g in a D-dimensional system of N particles where energy is dissipated only by rupture of capillary bridges. The two-dimensional calculation for a dry granular gas which obeys Haff's law can be found in [8, pp. 51-53, 115-118]. The results of the following calculation – similar to Haff's law – in three dimensions with dissipation only by rupture of capillary bridges and a comparison with numerical simulations can be found in [45–47].

In D dimensions we define granular temperature as

$$\frac{D}{2} T_g = \frac{1}{N} \sum_{i=1}^{N} \frac{m \mathbf{v}_i^2}{2}. \tag{3.1}$$

It is equal to the average kinetic energy for the case $D = 2$.

Assuming a homogeneous spatial distribution of particles, the total number of

collisions in our system during a time interval Δt is

$$\frac{f_{\text{coll}} N \Delta t}{2}, \tag{3.2}$$

where f_{coll} and N are the collision frequency (per particle and unit time), and number of particles, respectively. Division by 2 accounts for double-counting, as two particles are involved in each collision.

The kinetic energy decreases by the rupture energy E_{cb} for each bond that breaks, which occurs after collisions with a bond breaking probability P_{bb}. The total energy loss in an interval Δt is therefore given by [45, p. 87]

$$\Delta E_{\text{kin}} = -E_{cb} \frac{f_{\text{coll}} N \Delta t}{2} P_{\text{bb}}. \tag{3.3}$$

Division by N and Δt results in

$$\frac{1}{N} \frac{\Delta E_{\text{kin}}}{\Delta t} \overset{(3.1)}{=} \frac{D}{2} \frac{\Delta T_g}{\Delta t} = -\frac{1}{2} f_{\text{coll}} E_{cb} P_{\text{bb}}. \tag{3.4}$$

Under the assumption that sufficiently many collisions are happening per unit time, we can take the limit $\Delta t \to 0$ and we get the following differential equation:

$$\frac{D}{2} \frac{\mathrm{d}T_g}{\mathrm{d}t} = -\frac{1}{2} f_{\text{coll}} \Delta E P_{\text{bb}}. \tag{3.5}$$

Estimation of collision frequency Consider the motion of a single spherical particle with velocity v and diameter d in time Δt, assuming all other particles are stationary. In three dimensions the particle will collide with all particles in a cylinder of length $\langle v \rangle_{\Delta t} \Delta t$ and base area equal to the scattering cross section $\sigma_{3D} = \pi d^2$. In two dimensions the collision volume is a rectangle of the same length and width $\sigma_{2D} = 2d$. The number of collisions is

$$N_{\text{coll}} = n \sigma \langle v \rangle_{\Delta t} \Delta t, \tag{3.6}$$

where $n = \frac{N}{V}$ is the number density and V the volume/area of the system.

As the other particles are actually moving, we need to consider the relative velocity between particles. With the average relative velocity $\langle v_{\text{rel}} \rangle$ we obtain:

$$f_{\text{coll}} = \frac{N_{coll}}{\Delta t} = n \sigma \langle v_{\text{rel}} \rangle \tag{3.7}$$

We need an estimate for the average relative velocity. Assuming the particle velocities follow the Maxwell-Boltzmann distribution function

$$f(\mathbf{v}) = \left(\frac{m}{2\pi k T_g}\right)^{\frac{D}{2}} \exp\left(-\frac{m\mathbf{v}^2}{2kT_g}\right), \tag{3.8}$$

where k is the Boltzmann constant, the general expression for the average velocity is

$$\langle v \rangle = \int_{\text{all } \mathbf{v}} |\mathbf{v}| f(\mathbf{v})\, \mathrm{d}\mathbf{v}. \tag{3.9}$$

The respective coordinate transformation of (3.9) to the velocity magnitude is

$$\langle v \rangle = \int_0^\infty v F(v) dv. \tag{3.10}$$

Transforming (3.9) to spherical coordinates in the case $D = 3$ and integrating over the angles yields an additional factor equal the surface $4\pi v^2$ of a sphere of magnitude v:

$$F_{3D}(v)\, \mathrm{d}v = 4\pi v^2 \left(\frac{m}{2\pi k T_g}\right)^{\frac{3}{2}} \exp(-\frac{mv^2}{2kT_g})\, \mathrm{d}v. \tag{3.11}$$

In the case $D = 2$ transformation to polar coordinates yields a factor equal to the circumference $2\pi v$ of a circle of radius v. The resulting probability distribution function is

$$F_{2D}(v)\, \mathrm{d}v = \frac{m}{kT_g} v \exp\left(-\frac{mv^2}{2kT_g}\right)\, \mathrm{d}v. \tag{3.12}$$

Inserting (3.11) and (3.12) in (3.10) we obtain the average velocity

$$\langle v \rangle = \begin{cases} \sqrt{\frac{8kT_g}{\pi m}}\,, & D = 3 \\ \sqrt{\frac{\pi kT_g}{2m}}\,, & D = 2. \end{cases} \tag{3.13}$$

The general expression for the average relative velocity of two colliding particles is similar to (3.9), but involves the two-particle distribution function f_2:

$$\langle v_{\text{rel}} \rangle = \int_{\text{all } \mathbf{v}_1} \int_{\text{all } \mathbf{v}_2} |\mathbf{v}_1 - \mathbf{v}_2| f_2(\mathbf{v}_1, \mathbf{v}_2)\, \mathrm{d}\mathbf{v}_1\, \mathrm{d}\mathbf{v}_2. \tag{3.14}$$

An approximation for f_2 suggested by Enskog [8, p. 59] assumes correlation just in space and no correlations in velocity. The two-particle distribution function becomes the product of the two single-particle velocity distribution functions and the *pair*

correlation function or *radial distribution function* $g_2(r)$:

$$f_2(\mathbf{v}_1, \mathbf{v}_2) \approx g_2(r) f(\mathbf{v}_1) f(\mathbf{v}_2). \tag{3.15}$$

The pair correlation function describes the probability that a pair of particle is at distance r from each other. As the distance between the particle centers of two colliding particles is the diameter d, we use the value of the correlation function at contact $g_2(d)$. Using this approximation (3.14) becomes

$$\langle v_{\mathrm{rel}} \rangle = g_2(d) \int_{\text{all } \mathbf{v}_1} \int_{\text{all } \mathbf{v}_2} |\mathbf{v}_1 - \mathbf{v}_2| f(\mathbf{v}_1) f(\mathbf{v}_2) \, \mathrm{d}\mathbf{v}_1 \, \mathrm{d}\mathbf{v}_2. \tag{3.16}$$

Inserting the long form of the absolute relative velocity

$$|\mathbf{v}_1 - \mathbf{v}_2| = \sqrt{(\mathbf{v}_1 - \mathbf{v}_2)^2} = \sqrt{\mathbf{v}_1^2 - 2\mathbf{v}_1\mathbf{v}_2 + \mathbf{v}_2^2} \tag{3.17}$$

we obtain

$$v_{\mathrm{rel}} = g_2(d) \int_{\text{all } \mathbf{v}_1} \int_{\text{all } \mathbf{v}_2} \sqrt{\mathbf{v}_1^2 - 2\mathbf{v}_1\mathbf{v}_2 + \mathbf{v}_2^2} f(\mathbf{v}_1) f(\mathbf{v}_2) \, \mathrm{d}\mathbf{v}_1 \, \mathrm{d}\mathbf{v}_2. \tag{3.18}$$

Working out the integral under the assumption that $\mathbf{v}_1$ and $\mathbf{v}_2$ are uncorrelated, one finds

$$\langle v_{\mathrm{rel}} \rangle = g_2(d) \sqrt{2} \cdot \langle v \rangle \, . \tag{3.19}$$

Inserting the average velocity from (3.13) we get an estimate for the average relative velocity

$$\langle v_{\mathrm{rel}} \rangle = \begin{cases} 4 g_2(d) \sqrt{\frac{k T_g}{\pi m}} \, , & D = 3 \\ g_2(d) \sqrt{\frac{\pi k T_g}{m}} \, , & D = 2 \end{cases} \tag{3.20}$$

and the collision frequency [47]

$$f_{\mathrm{coll}} = \begin{cases} 4 g_2(d) \sigma_{3D} n \sqrt{\frac{k T_g}{\pi m}} \, , & D = 3 \\ g_2(d) \sigma_{2D} n \sqrt{\frac{\pi k T_g}{m}} \, , & D = 2. \end{cases} \tag{3.21}$$

Early stage of cooling During the early stage of cooling the particle energies are still much larger than the bridge rupture energy. We can assume that the bond

breaking probability $P_{\text{bb}} \approx 1$. Inserting this and (3.21) into (3.5) yields

$$\frac{\mathrm{d}T_g}{\mathrm{d}t} = -\frac{1}{D}\Delta E = f_{\text{coll}} \overset{(3.21)}{=} \begin{cases} -\frac{4}{3}E_{cb}g_2(d)d^2n\sqrt{\frac{\pi kT_g}{m}}\ , & D=3 \\ -E_{cb}g_2(d)dn\sqrt{\frac{\pi kT_g}{m}}\ , & D=2. \end{cases} \tag{3.22}$$

Differential equations of the form $\frac{\mathrm{d}T}{\mathrm{d}t} \propto -\sqrt{T}$ are solved by $T(t) \propto (t-t_0)^2$. Solving with the initial condition $T_g(0) = T_0$ we get

$$T_g(t) = \begin{cases} T_0(1-t/t_0)^2 & \text{if } t \le t_0 \\ 0 & \text{if } t > t_0 \end{cases} \tag{3.23}$$

with the characteristic time scale

$$t_0 = \begin{cases} \frac{3}{2g_2(d)\sigma_{3D}nE_{cb}}\sqrt{\frac{\pi mT_0}{k}}\ , & D=3 \\ \frac{4}{g_2(d)\sigma_{2D}nE_{cb}}\sqrt{\frac{mT_0}{\pi k}}\ , & D=2. \end{cases} \tag{3.24}$$

The resulting temperature decay is similar to Haff's law for the temperature decay of a dry granular gas of initial temperature T_0 [8, 23],

$$T(t) = \frac{T_0}{(1+t/\tau_0)^2}, \tag{3.25}$$

where $\tau_0^{-1} \propto nd^2(1-\varepsilon^2)\sqrt{T_0}$.

For hard spheres ($D=3$) we can use [8, p. 59]

$$g_2(d) = \frac{2-\eta}{2(1-\eta)^3}, \tag{3.26}$$

where $\eta = n\frac{1}{6}\pi d^3$ is the packing fraction or volume fraction. For hard disks ($D=2$)

$$g_2(d) = \frac{1-(7/16)\eta}{(1-\eta)^2}, \tag{3.27}$$

with $\eta = n\frac{1}{4}\pi d^2$ [8, p. 116].

At this point we have a theoretical prediction for the early stage of cooling. A more detailed discussion of free cooling, including the late phase of cooling, can be found in [44].

Simulation results for the decay of temperature over time are shown in Fig. 3.1. If the theoretical prediction for the characteristic time scale t_0 (3.24) is multiplied

by 1.4, the data points lie on the resulting curve.

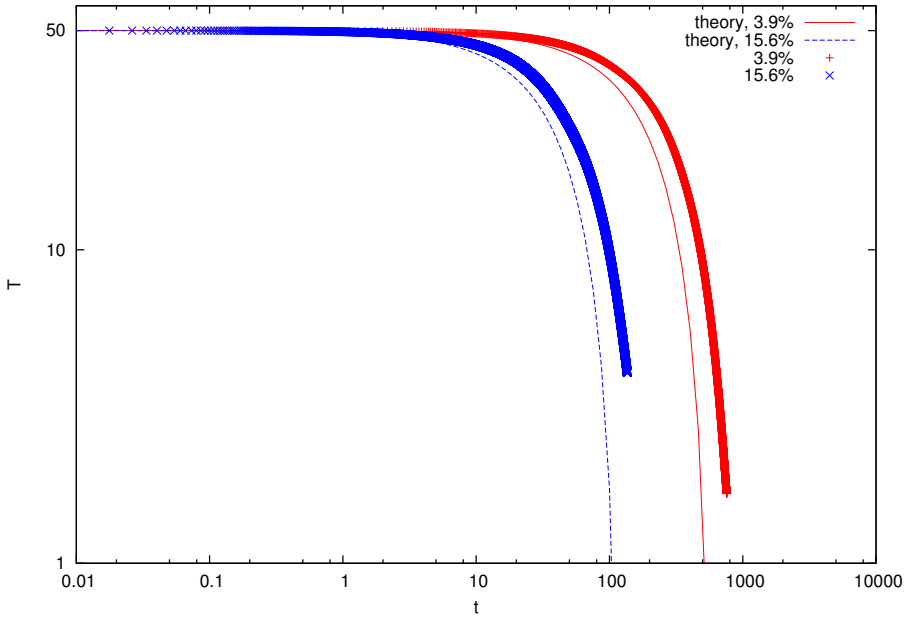

Figure 3.1: Free cooling in two-dimensional event-driven molecular dynamics simulations of $N = 10^4$ particles. Temperature is plotted over time on double-logarithmic axis. The system is quadratic ($L_x = L_y = L$) with periodic boundary conditions and variable area fraction $\phi = \frac{N \cdot \pi R^2}{L^2}$. The parameters were chosen as in [46]: rupture energy $E_{cb} = 1$, rupture distance $s_{\text{crit}} = 0.28$, coefficient of restitution $\varepsilon = 1$, initial temperature $T_0 = 50$, particle radius $R = 2$. Simulations of two different area fractions $\phi = 3.9\%$ and $\phi = 15.6\%$ are compared with their theoretical prediction (3.23).

4 Granular Phase Diagram

4.1 Phase Diagrams

In time-driven simulations performed by Klaus Röller using sinusoidally moving walls, slightly polydisperse particles ($\sigma_p = 0.06$) with average diameter $d = 1$, and gravitational acceleration $g = 1$, he observed different states (Fig. 4.1), depending on two control parameters.

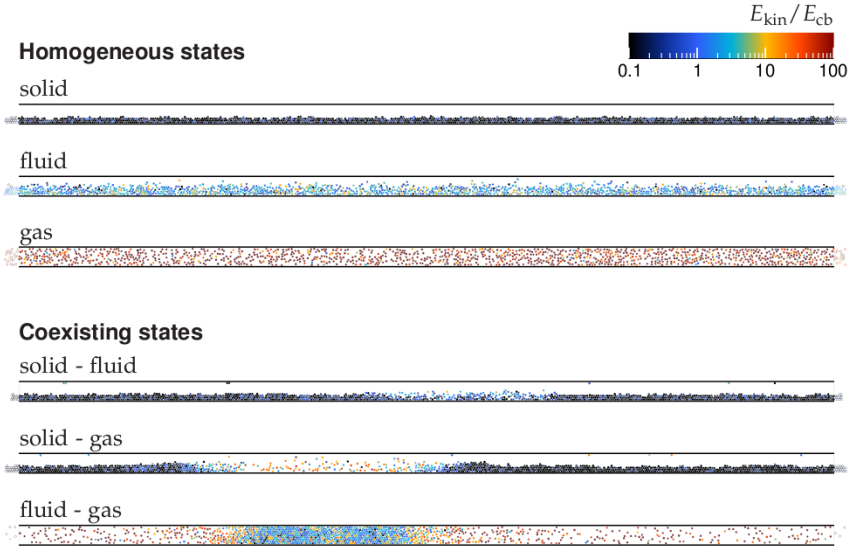

Figure 4.1: States of wet granular matter [41]. Two-dimensional time-driven molecular dynamics simulations were performed using the minimal capillary model. The system of $1.2 \cdot 10^3$ slightly polydisperse ($\sigma_p = 0.06$) particles with mean diameter $d = 1$ in a box of size $9d \times 400d$ as sketched in Fig. 4.3. Shaking is performed in vertical direction, gravity points downward ($g = 1$). The capillary bridge energy is $E_{cb} = 1.14$. The phase states depend on the driving parameters peak acceleration Γ and driving energy E^*.

The sinusoidal driving $z(t) = A\cos(\omega t)$ (see Fig. 1.3) is characterized by its am-

plitude A and angular frequency ω. Driving can be characterized by other control parameters as well. The control parameter chosen in [17] is the maximum kinetic energy a particle can obtain from the collision with a wall:

$$E_{\max} = \frac{1}{2} m v_{\max}^2 = \frac{1}{2} m (A\omega)^2, \tag{4.1}$$

with the mass of a particle m and the maximum velocity of the wall,

$$v_{\max} = \max\left(\frac{\mathrm{d}z(t)}{\mathrm{d}t}\right) = A\omega. \tag{4.2}$$

Klaus Röller chose to normalize this parameter with the capillary bridge energy and used the dimensionless control parameter

$$E^* = \frac{E_{\max}}{E_{cb}}. \tag{4.3}$$

The other dimensionless control parameter is the maximum acceleration of a particle, normalized with respect to the gravitational acceleration g:

$$\Gamma = \frac{\max\left(\frac{\mathrm{d}^2 z(t)}{\mathrm{d}t^2}\right)}{g} = \frac{A\omega^2}{g} \tag{4.4}$$

These equations show that the parameters E^* and Γ can be controlled independently by varying the driving amplitude A and angular frequency ω.

It turned out to be enlightening to plot the phases and phase transitions in the plane spanned by Γ and E^* [41]. The resulting phase diagram for $\frac{E_{cb}}{mgs_{\mathrm{crit}}} = 4.0$ is shown in Fig. 4.2. Low values of the peak acceleration lead to a solid phase, mostly independent of the driving energy. The particles lie on the moving ground plate and follow its sinusoidal movement without being accelerated enough to lift from the ground. For higher driving energies, there are two kinds of solid-gas coexistence. One is depicted in Fig. 4.1. The other is called granular Leidenfrost effect (see [17]), where particles close to the ground absorb the driving energy in a gas state and a solid phase is floating on top of the gas bubble. Low driving energies at high peak acceleration result in a liquid phase (denoted as *fluid* in the phase diagram), where particles are moving, but the density is high and they are not filling the whole system volume (see Fig. 4.1). High driving energies at high peak acceleration result in a gas state. The solid red line is a theoretical prediction for the solid-liquid transition, derived in Ref. [41, chapter 4]. Between the liquid and the gas state

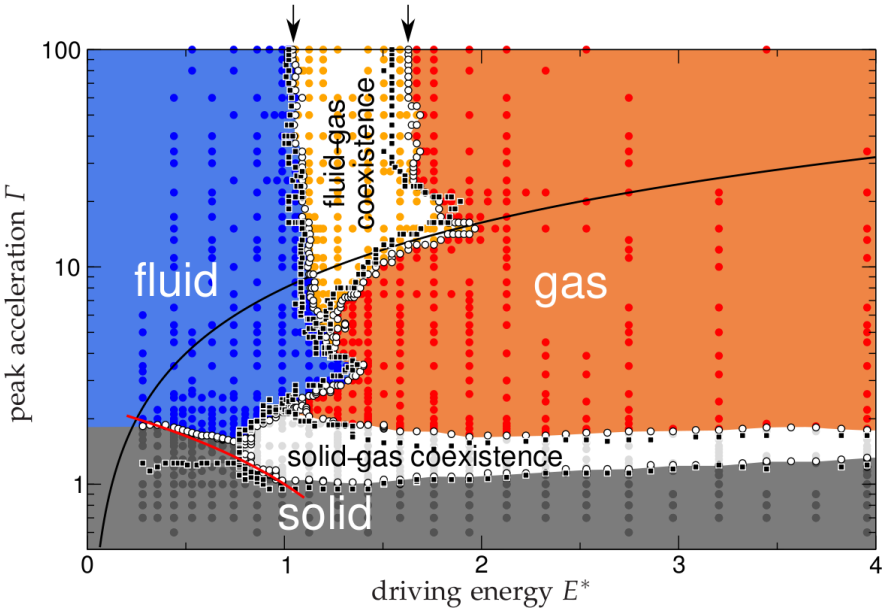

Figure 4.2: Phase diagram of agitated wet granular matter [41] from simulations with 1200 particles in two dimensions. Circles denote time-driven simulations (minimal capillary model), squares denote event-driven simulations (thin-thread model). The solid red line is a theoretical prediction for the solid-liquid transition. At the solid black curve the excitation amplitude A equals the capillary bridge rupture length s_{crit}.

there is a liquid-gas coexistence regime. The critical values of E^* for the vertical liquid-gas boundaries are indicated by arrows at the top. At the solid black curve the excitation amplitude A equals the capillary bridge rupture length s_{crit}. This curve seems to be the lower boundary for liquid-gas coexistence. Below the black curve, $A > s_{\mathrm{crit}}$. The reasons and requirements for the existence of this coexistence regime are not yet understood.

The goal of the following section is to establish a minimal model that can be used as a starting point for a further characterisation of the coexistence regimes.

4.2 Minimal Model

The required elements of our minimal model have been introduced in chapter 2. We perform event-driven molecular dynamics simulations of a dilute system of wet granular matter in two-dimensions. N particles of equal diameter, d, and equal mass, m, are filled in a flat box of length L_x and height L_y having periodic bound-

ary conditions in horizontal direction. The reflecting walls in vertical direction are heated walls according to section 2.3.3. The system is sketched in Fig. 4.3. It needs

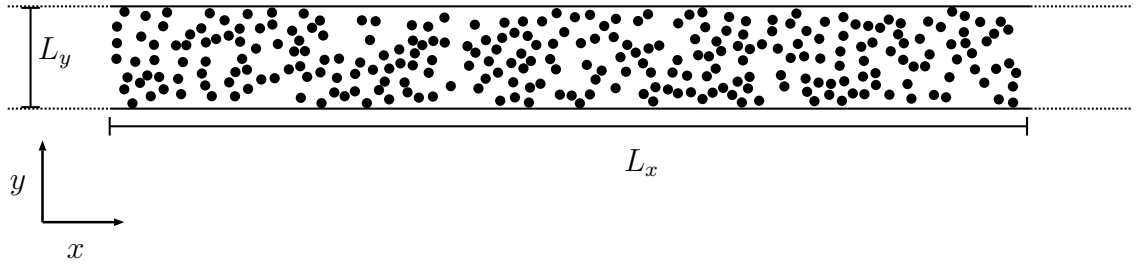

Figure 4.3: Sketch of the two-dimensional simulation system. Particles of diameter d are filled in a flat box ($L_y = 9d$) with periodic boundary conditions in horizontal direction ($L_y = 400d$, if not noted otherwise), and heated, reflecting walls in vertical direction. Note that the actual systems are much longer in horizontal direction.

to be flat to ensure homogeneous vertical density and good coupling of the whole system to the walls.

For simplicity, particle-particle and particle-wall-collisions are elastic, i.e., $\varepsilon = 1$ and $\varepsilon_{\text{wall}} = 1$. Moreover, units are chosen such that the particle mass is $m = 1$, their diameter $d = 1$, and the Boltzmann constant is $k = 1$. In order to simplify the prospective theoretical description, there is no gravitational acceleration ($g = 0$). Capillary bridges are formed between particles as well as between particle and wall. The numerical values for rupture energy $E_{cb} = 0.2844$, and rupture distance $s_{\text{crit}} = 0.0711d$, as well as the system height $L_y = 9d$, coincide with Röller's choice [41], and are matched to the experiment described in chapter 1. Initially the particles are uniformly distributed over the whole system with random velocities, normalized to result in a given initial granular temperature T_0.

4.3 Simulation Results

All results presented in this section were obtained using the minimal model described in the previous section.The control parameter of the wall model is E_{wall}. We define the driving energy for this model as $E^* = \frac{E_{\text{wall}}}{E_{cb}}$.

We are interested in the time evolution of coarse-grained quantities like density and temperature. A local number density, averaged in vertical direction, is obtained by counting particles in a given interval (bin). The local temperature is obtained

analogously, by averaging over the temperatures of all particles inside the bin. The areal density is obtained by division of the time averaged particle number density over the maximum number density at cubic packing. The time-averaging interval is $\Delta t = 0.1$, the spatial binsize is $\Delta x = 4$ in all following space-time plots.

4.3.1 Solid ($E^* = 1.42$)

Figure 4.4 shows snapshots of the system using a driving energy $E^* = 1.42$ inspired by Fig. 4.2. As there is no gravitational acceleration, and wall positions are constant over time, the coupling to the energy-injecting walls is obviously different. Particles

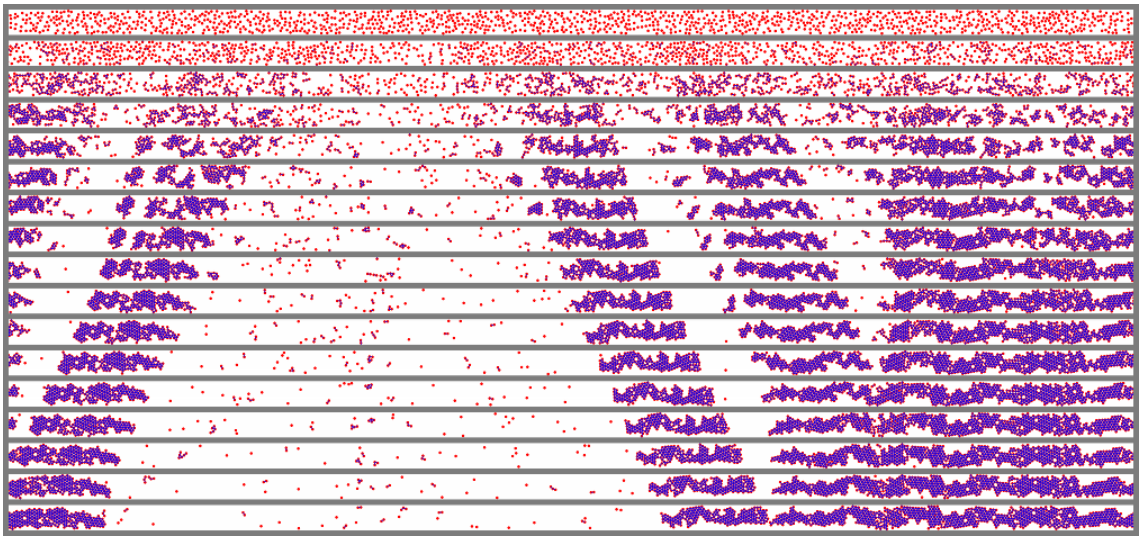

Figure 4.4: Snapshots of a simulation with $N = 1200$ particles, box width $L_x = 400d$, $L_y = 9d$, initial temperature $T_0 = 20E_{cb}$, and driving energy $E^* = 1.42$. Starting at $t = 0$, each snapshot was taken after 10^5 events. Particles are depicted as red circles, capillary bridges are shown as blue lines connecting the particle centers. Particles cluster in initially slighty denser regions, forming five dense regions in this case. Subsequently, coarsening results in an approaching and merging of these regions. Moving towards each other, the clusters form a single large cluster with crystal-like structure.

cluster in initially slighty denser regions, forming five dense regions visible in the first few snapshots. Coarsening results in an approaching and merging of these regions, until there is only one remaining cluster.

At later times of this system, no particles are moving freely. Particles that detach from the cluster reattach again at their next collision. The large cluster looks like

multiple solid blocks connected by flexible hinges at regions with lower density in vertical direction. This leads to a snake-like motion in animations. The solid blocks move towards a wall until the particle closest to the wall collides. At this point the block changes its vertical direction. Doing so, the energy injected into the system by the heated wall is dissipated via rupturing bridges in the "hinges".

Fig. 4.5 shows the evolution of areal density and temperature in dependence of the lateral position x over time, obtained by coarse-graining as described above. The plots are presented in both logarithmic and linear time scale to give a better impression of both early and long time evolution. In the areal density plot one can see the movement of single particles in the low density region. The "hinges" can be seen as stripes of lower density (around 0.5) next to stripes of higher density (close to 1). The movement of single particles is visible more clearly in the temperature plot. The dense phase is almost invisible, because its temperature is very low.

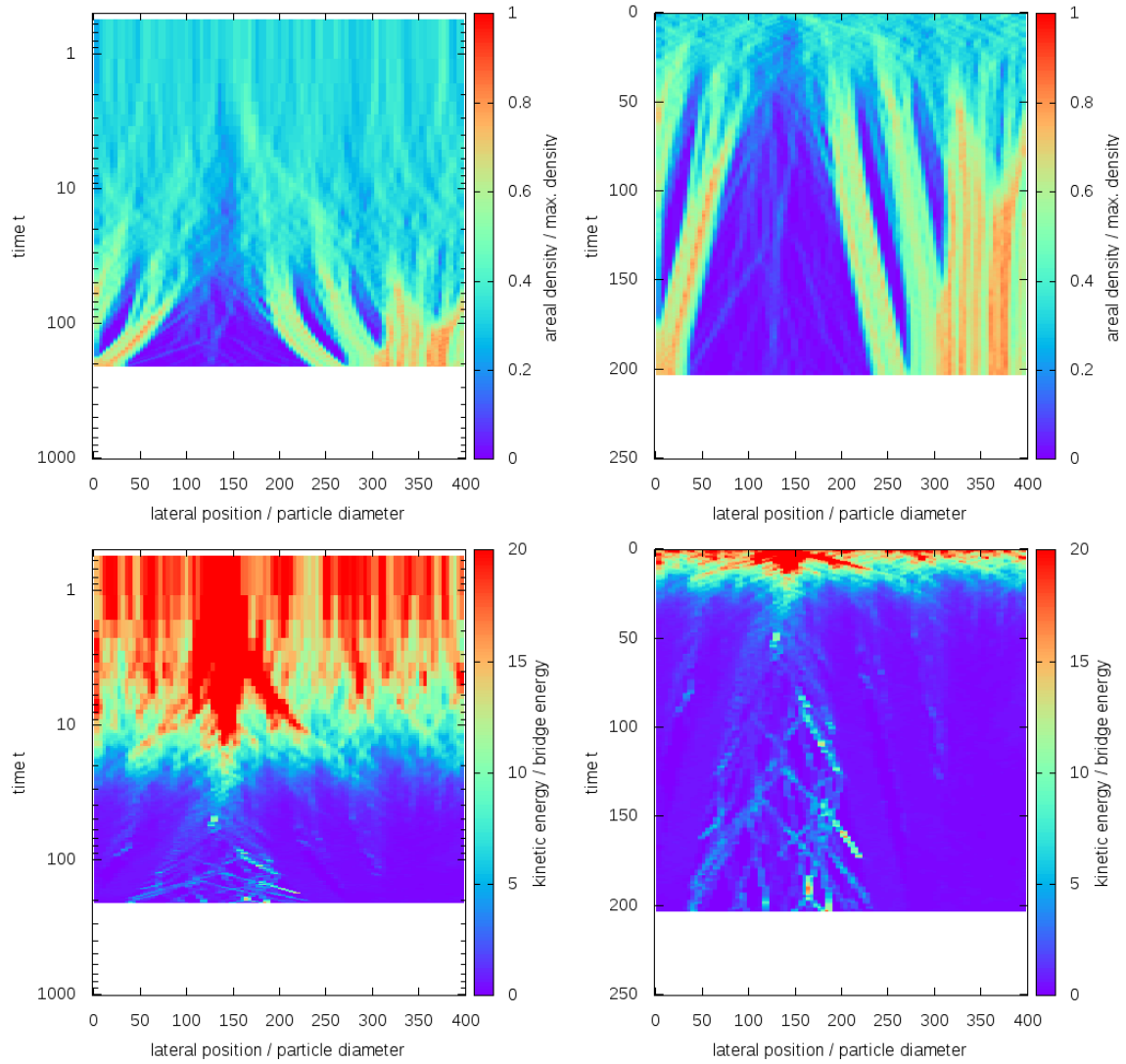

Figure 4.5: Areal density (color) in a space-time plot on logarithmic (top left) and linear (top right) time scale. Local temperature (color) in a space-time plot on logarithmic (bottom left) and linear (bottom right) time scale. The parameters are $N = 1200$, $L_x = 400d$, $L_y = 9d$, $T_0 = 20E_{cb}$ and $E^* = 1.42$.

4.3.2 Solid-Gas Coexistence ($E^* = 3.195$)

Increasing the driving energy, we obtain a nonzero density in the region not populated by the cluster, also for greater system time (Fig. 4.7). At the early stage of coarsening, there are approximately 25 dense regions that form a single dense region surrounded by gas at $t \approx 100$. In the center of Fig. 4.7 the capillary bridge density of the system as a function of lateral position and time (averaged over vertical position) is shown. It was obtained as described before for the areal density and temperature. The maximum value of 6 is achieved if a particle has capillary bridges with the maximum number of 6 neighbours. A capillary bridge between two particles is counted once for each particle. Fig. 4.6 shows a snapshot of the

Figure 4.6: Snapshot ($t \approx 970$) of the system showing liquid-gas coexistence. The logarithmic color coding is chosen similar to Fig. 4.1, but with a maximum value of 10. Capillary bridges are drawn as light blue lines connecting particle centers. The parameters are $N = 1200$, $L_x = 400d$, $L_y = 9d$, $T_0 = 20E_{cb}$ and $E^* = 3.195$.

system before the solid phase reaches a steady state. At its right boundary a lower density region can be seen, which also shows as low density region in Fig. 4.7. The solid phase clearly shows a high amount of capillary bridges (light blue lines) and crystal-like structure as Fig. 4.4, but actually covers the whole vertical space.

Figure 4.7: Areal density (color) in a space-time plot on logarithmic (top left) and linear (top right) time scale. Regions of lower density inside the cluster ("hinges"), as described for the solid phase in section 4.3.1, can be observed as lines over time. Capillary bridge density (color) in a space-time plot on logarithmic (center left) and linear (center right) time scale. For $t < 10$, capillary bridges do not persist over time. Local temperature (color) in a space-time plot on logarithmic (bottom left) and linear (bottom right) time scale. The kinetic energy is equal to the granular temperature in two dimensions (Eq. (3.1)). It is normalized by the rupture energy E_{cb}. The solid cluster has a homogeneus very low kinetic energy. The strong fluctuations in the remaining system are caused by few particles moving around at high kinetic energies. The parameters are $N = 1200$, $L_x = 400d$, $L_y = 9d$, $T_0 = 20E_{cb}$ and $E^* = 3.195$.

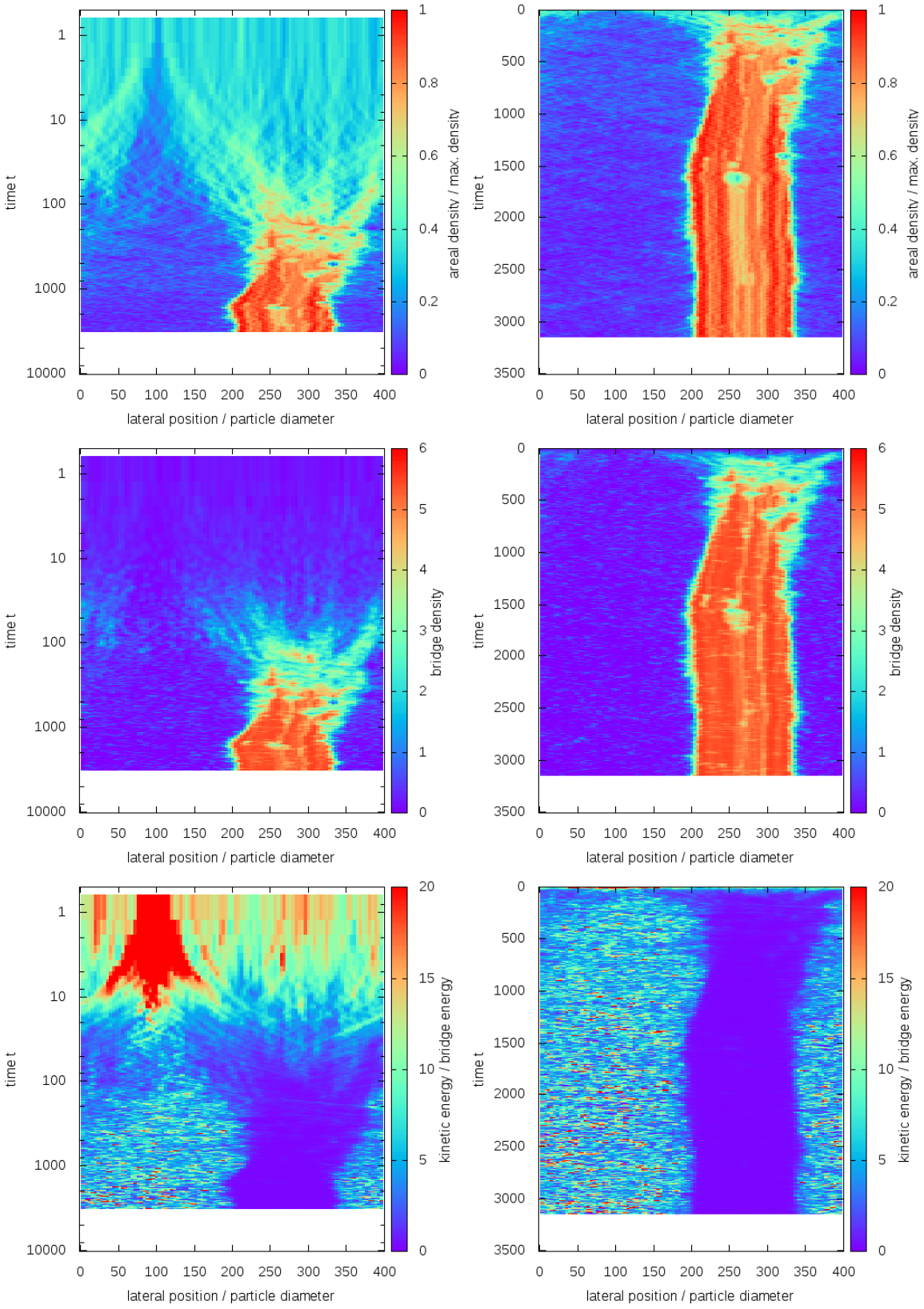

Figure 4.7: Caption on previous page.

4.3.3 Liquid-Gas Coexistence ($E^* = 3.55$)

For the driving energy $E^* = 3.55$, we observe liquid-gas coexistence (Fig. 4.8).

Figure 4.8: Snapshot ($t \approx 920$) of the system showing liquid-gas coexistence. The logarithmic color coding is chosen similar to Fig. 4.1, but with a maximum value of 10. Capillary bridges are drawn as light blue lines connecting particle centers. The parameters are $N = 1200$, $L_x = 400d$, $L_y = 9d$, $T_0 = 20E_{cb}$ and $E^* = 3.55$.

For $t < 100$, particles are moving towards a region of higher density (Fig. 4.9, top left). On the reviewed timescale the region of higher density seems to be stable, like in a steady state. Both phases are in motion. The density fluctuations of the less dense phase are faster than the fluctuations in the more dense phase. Formation of capillary bridges seems to happen in the same time scale as in the system showing higher density (Fig. 4.7), but does not reach high values that remain stable over time. Lower bridge density indicates a higher mobility. Most of the system cooled down from the initial temperature $T_0 = 20E_{cb}$ faster than the time resolution can resolve. The shape of the region of low kinetic energy ($t \lesssim 10$) looks very similar to the shape of high bridge density (Fig. 4.9, top and bottom left).

Figure 4.9: Areal density (color) in a space-time plot on logarithmic (top left) and linear (top right) time scale. Capillary bridge density (color) in a space-time plot on logarithmic (center left) and linear (center right) time scale. Local temperature (color) in a space-time plot on logarithmic (bottom left) and linear (bottom right) time scale. The parameters are $N = 1200$, $L_x = 400d$, $L_y = 9d$, $T_0 = 20E_{cb}$ and $E^* = 3.55$.

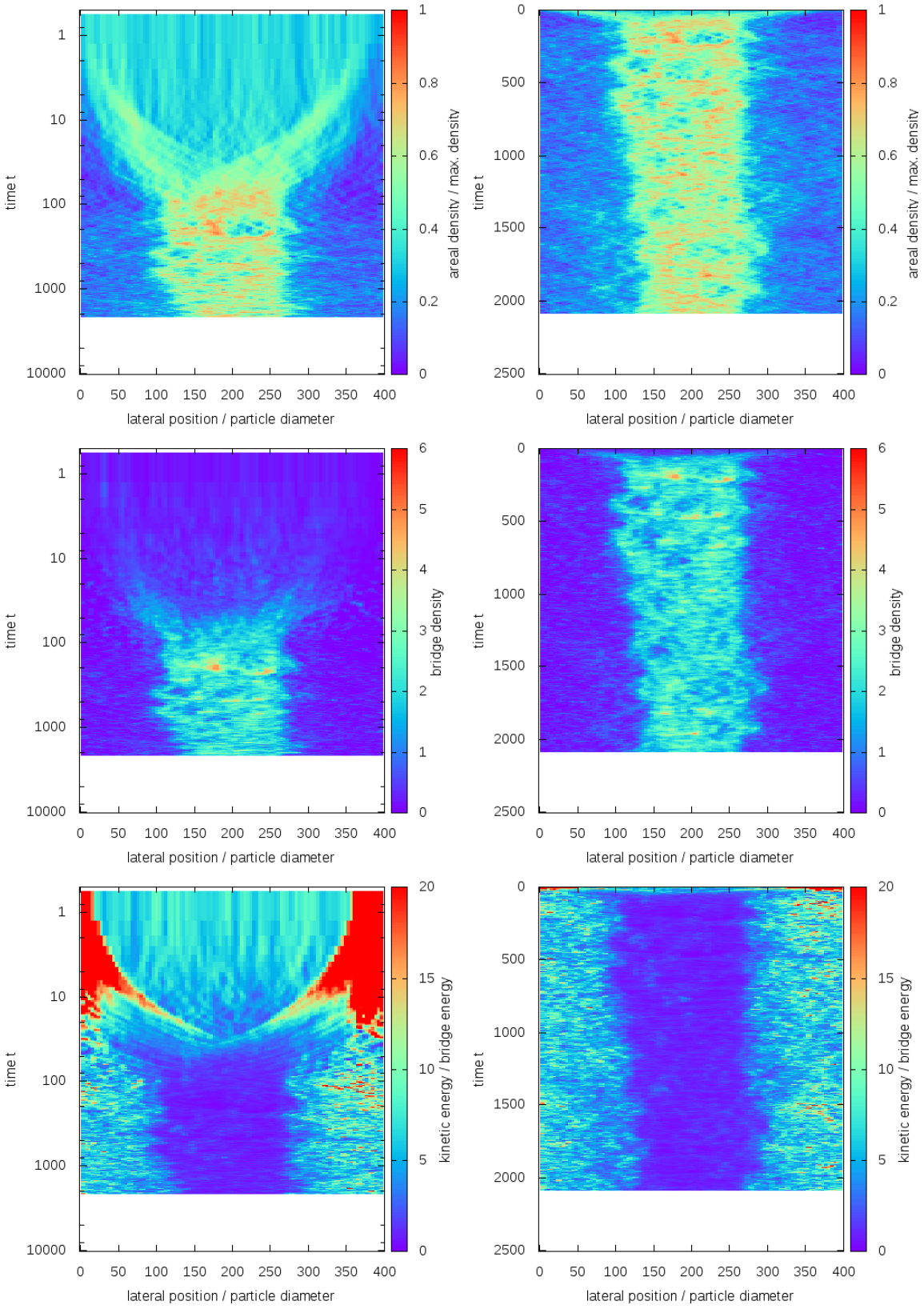

Figure 4.9: Caption on previous page.

4.3.4 Granular Gas ($E^* = 4.26$)

For high driving energy $E^* = 4.26$ we observe a granular gas (Fig. 4.10). The system shows severe density fluctuations, but there is no distinguishable structure.

Particles are distributed almost homogeneously over the system. At this driving energy there are no persistent capillary bridges. At lateral position $x \approx 300$ there might be the onset of a distinguishable phase. The kinetic energy is slightly lower at lateral position $x \approx 300$, matching the area of slightly higher bridge density in Fig. 4.10.

Figure 4.10: Areal density (color) in a space-time plot on logarithmic (top left) and linear (top right) time scale. Capillary bridge density (color) in a space-time plot on logarithmic (center left) and linear (center right) time scale. Local temperature (color) in a space-time plot on logarithmic (bottom left) and linear (bottom right) time scale. The system is in a steady state with severe density flucuations. The parameters are $N = 1200$, $L_x = 400d$, $L_y = 9d$, $T_0 = 20E_{cb}$ and $E^* = 4.26$.

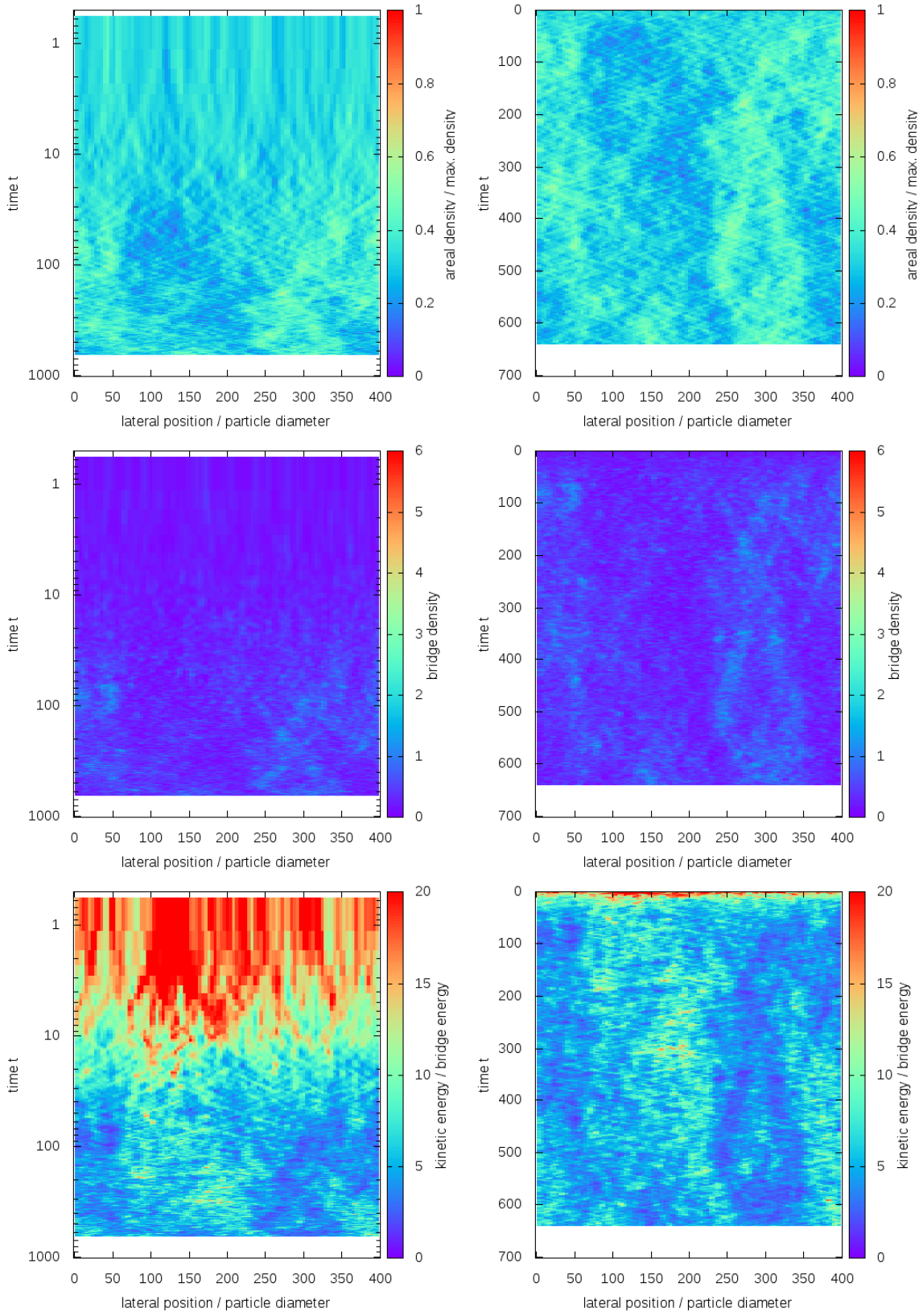

Figure 4.10: Caption on previous page.

4.3.5 Consistency Checks

The existence of the more dense liquid phase should not depend on the initial temperature. This is checked by a simulation with the same parameters and driving energy that showed liquid-gas coexistence ($E^* = 3.55$), but much higher initial temperature $T_0 = 200E_{cb}$ (Fig. 4.11).

For $t > 100$ the system looks like the results for the same parameters with lower initial temperature (Fig. 4.9), shifted over the periodic boundary as the position of the dense phase should be random. Cooling is happening on a larger time interval. If one would be drawing a curve beginning at the boundary between high and low density (at $t = 0$ it begins at $x \approx 250$) moving along equal density, this curve seems to cross the dense phase up to the other side of the dense phase. The two curves are more clear at very small times in Fig. 4.9, the crossing of both curves is more clear in the current figure. The bridge density looks like Fig. 4.9, but having a later onset of higher density in Fig. 4.11. Note that the color scale in the logarithmic plot of the temperature is different, because the initial temperature is much higher than the steady state temperature. After the initial cooling phase it looks like Fig. 4.9, shifted over the periodic boundary.

Figure 4.11: Areal density (color) in a space-time plot on logarithmic (top left) and linear (top right) time scale. Capillary bridge density (color) in a space-time plot on logarithmic (center left) and linear (center right) time scale. Local temperature (color) in a space-time plot on logarithmic (bottom left) and linear (bottom right) time scale. The driving energy $E^* = 3.55$ like in Fig. 4.9, but at higher initial temperature $T_0 = 200E_{cb}$. Note that the color scale in the logarithmic plot is different as the initial temperature is much higher than the steady state temperature. The parameters are $N = 1200$, $L_x = 400d$, $L_y = 9d$, $T_0 = 200E_{cb}$ and $E^* = 3.55$.

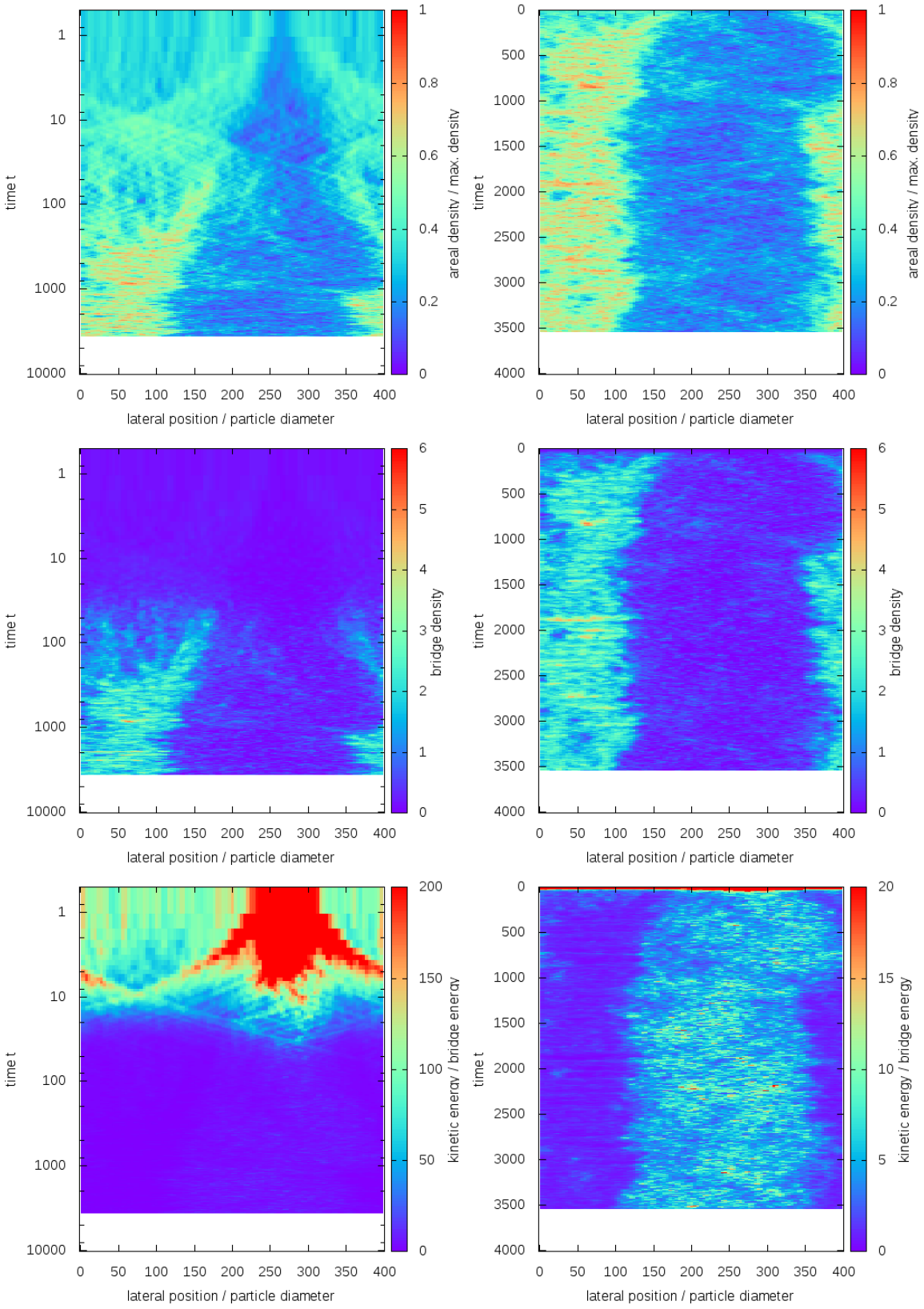

Figure 4.11: Caption on previous page.

If the control parameter E^* was an extensive order parameter, the previous system should show the same behaviour at constant density and higher volume. Simulation results of a system twice as wide are presented in Fig. 4.12.

The early stage ($t < 11$) looks similar to the previous density plots on a slightly different time scale. After crossing of the two boundary curves there are more dense regions aggregating to a very dense, stable phase. In the observed timeframe there are three distinguishable phases. The bridge density does not show high density regions at $11 < t < 100$. For $t > 100$ the bridge density also has regions of three distinguishable types and shows the same low density "bubbles" as the areal density.

Figure 4.12: Areal density (color) in a space-time plot for $E^* = 3.55$ in a system twice as wide ($L_x = 800d$) as in Fig. 4.11 at equal density ($N = 2400$) on logarithmic (top left) and linear (top right) time scale. Capillary bridge density (color) in a space-time plot on logarithmic (center left) and linear (center right) time scale. Local temperature (color) in a space-time plot on logarithmic (bottom left) and linear (bottom right) time scale. Note that the color scale in the logarithmic plot is different as the initial temperature is much higher than the steady state temperature. The parameters are $N = 2400$, $L_x = 400d$, $L_y = 9d$, $T_0 = 200E_{cb}$ and $E^* = 3.55$.

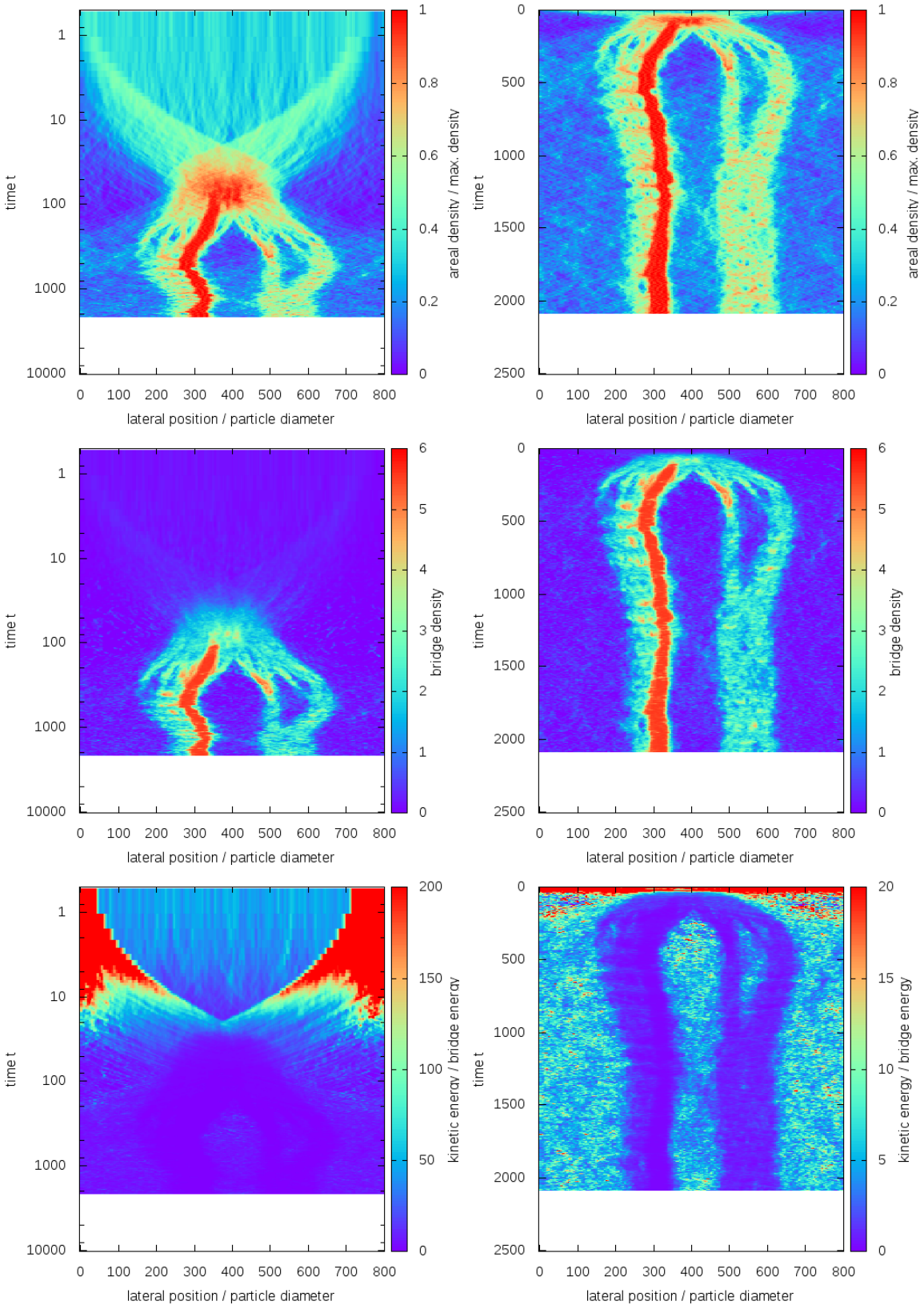

Figure 4.12: Caption on previous page.

5 Discussion and Outlook

Our minimal model has proven to be sufficient to capture phase transitions and coexistence in wet granular matter: for increasing energy input we observed solid-like, liquid-like, and granular gas phases.

One way of distinguishing between homogeneous fluid and solid phases is the quantification of particle mobility by calculating a dynamic order parameter called *frequency of location changes*. A location change is happening, if the vectorial area of a particle's Voronoi cell changes sign, because it moved into the Voronoi cell of another particle [41]. For our model and utilized parameters, the combination of the three reviewed quantities areal density, bridge density and temperature provide ample identification. Table 5.1 lists the value ranges we chose to distinguish between solid, liquid, and gas phase. Areal density and bridge density of the liquid phase show strong fluctuations than could also be taken into account as a unique feature.

In the model we observed solid-gas and liquid-gas coexistence. This is a very important result, because it means that neither gravitational acceleration nor oscillating walls are required for phase coexistence in wet granular matter.

From ordinary thermodynamics we expected that the temperature would be equal in coexisting phases. The surprising result is that phases showed different temperatures instead. We still expect the pressure to be equal between phases, because a difference in pressure would induce a particle flow from one phase to another, which we could not observe in the examined quantities. The particle flux at phase boundaries is another interesting quantity that could be measured in the future. For

	areal density	bridge density	T_g
solid	$\simeq 0.9$	> 4	$\lesssim 2E_{cb}$
liquid	$0.5 \ldots 0.9$	$1 \ldots 3$	$2 \ldots 4$
gas	< 0.7	< 1	$\gg E_{cb}$

Table 5.1: Value ranges for areal density, bridge density, and temperature, that can be used to identify and distinguish phases.

further investigation of phase interaction at their boundary, we will also look at the dissipated power, which is proportional to the bridge ruptures per unit time. We expect that this quantity shows illuminating singularities at the phase boundaries that will provide insight into the coexistance condition for granular phases with different granular temperature. Other interesting quantities which might help understanding boundary interaction are the mean free path and free time of particles close to the boundary. For the most recent simulations, this data is already present and needs to be analyzed.

If data is written and analyzed at higher time resolution for the coarsening behaviour at the beginning of the simulations, it would be an interesting challenge to check in how far this agrees with standard scenarios for Ostwald ripening like the Lifshitz-Slyozov theory of coarsening [30].

As the molecular interaction of the Van der Waals gas is similar to the interaction in models of granular matter with elastic collisions ($\epsilon = 1$), there have been attempts to find an equation of state for granular matter [20, 24] – although it is a non-equlibrium system. We could try to find an equation of state for the heated wall model.

Arguably, the most surprising result of our exploratory study was the observation of three phases coexisting in Fig. 4.12. It might be an artefact of crystallization or a transient state that disappears after longer simulation time, but it could also be a persistent feature: In private conversation Röller reported that indications into that direction were also observed in experiments.

Hence, there emerges here another striking difference between conventional and granular matter. In ordinary thermodynamics, the Gibbs phase rule describes the thermodynamic degrees of freedom f for a system with r components and M coexisting phases [10, p. 286]:

$$f = r - M + 2 \tag{5.1}$$

In a system with one component $r = 1$ and two coexisting phases $M = 2$ there is one degree of freedom resulting in a coexistence curve in the phase diagram, for example temperature as function of pressure. For three coexisting phases $M = 3$ there is no degree of freedom. The point in the phase diagram, at which three-phase coexistence exists, is called triple point. In our system the degrees of freedom might be the driving energy E^* and area fraction of the system $\phi = \frac{N}{L_x \cdot L_y}$. As it is not very likely that we found exactly the tricitical point by coincidence, in wet granular matter the three-phase coexistence might actually be an area rather than a triple

point.

The step that needs to be done next is running many simulations in small intervals of E^* and identification of the resulting phases (type and size). This leads to a one-dimensional phase diagram. Afterwards another dimension could be explored, for example the area fraction ϕ.

Censequently in this simple model, there will be a lot to discover, and one has to be ready for many surprises.

Bibliography

[1] B. J. Alder and T. E. Wainwright. Studies in Molecular Dynamics. I. General Method. *The Journal of Chemical Physics*, 31(2):459–466, 1959. doi: 10.1063/1.1730376.

[2] P. Allen and D. J. Tildesley. *Computer Simulation of Liquids*. Oxford Science Publications. Oxford University Press, USA, 1989. ISBN 9780198556459.

[3] R. Aveyard, J. H. Clint, V. N. Paunov, and D. Nees. Capillary condensation of vapours between two solid surfaces: effects of line tension and surface forces. *Phys. Chem. Chem. Phys.*, 1(1):155–163, 1999.

[4] I. Battiato and J. Vollmer. Fluidization of Wet Granulates under Hydrodynamic Shear. Technical Report arXiv:1105.2594, May 2011.

[5] F. Bertrand, L. A. Leclaire, and G. Levecque. DEM-based models for the mixing of granular materials. *Chemical Engineering Science*, 60(8):2517–2531, 2005.

[6] C. Bizon, M. D. Shattuck, J. B. Swift, W. D. McCormick, and H. L. Swinney. Patterns in 3d vertically oscillated granular layers: simulation and experiment. *Physical review letters*, 80(1):57–60, 1998.

[7] L. Bocquet, É. Charlaix, and F. Restagno. Physics of humid granular media. *Comptes Rendus Physique*, 3(2):207–215, 2002.

[8] N. V. Brilliantov and T. Pöschel. *Kinetic Theory of Granular Gases*. Oxford Graduate Texts. Oxford University Press, USA, 2004. ISBN 9780198530381.

[9] N. V. Brilliantov, F. Spahn, J. M. Hertzsch, and T. Pöschel. Model for collisions in granular gases. *Physical review E*, 53(5):5382, 1996.

[10] H. B. Callen. *Thermodynamics and an introduction to thermostatistics*. Wiley, 1985. ISBN 9780471862567.

[11] E. Clément, L. Vanel, J. Rajchenbach, and J. Duran. Pattern formation in a vibrated two-dimensional granular layer. *Physical Review E*, 53(3):2972, 1996.

[12] R. Dikau. *Landslide recognition: identification, movement, and clauses*. Publication (International Association of Geomorphologists). J. Wiley & Sons, 1996. ISBN 9780471964773.

[13] S. Douady, S. Fauve, and C. Laroche. Subharmonic instabilities and defects in a granular layer under vertical vibrations. *EPL (Europhysics Letters)*, 8:621, 1989.

[14] Y. Du, H. Li, and L. P. Kadanoff. Breakdown of hydrodynamics in a one-dimensional system of inelastic particles. *Physical review letters*, 74(8):1268–1271, 1995.

[15] J. Duran. *Sands, Powders, and Grains: An Introduction to the Physics of Granular Materials*. Partially Ordered Systems. Springer, 2000. ISBN 9780387986562.

[16] J. Duran. The physics of fine powders: plugging and surface instabilities. *Comptes Rendus Physique*, 3(2):217 – 227, 2002. ISSN 1631-0705. doi: 10.1016/S1631-0705(02)01313-0.

[17] P. Eshuis, K. van der Weele, D. van der Meer, and D. Lohse. Granular Leidenfrost effect: Experiment and theory of floating particle clusters. *Physical review letters*, 95(25):258001, 2005.

[18] É. Falcon, R. Wunenburger, P. Évesque, S. Fauve, C. Chabot, Y. Garrabos, and D. Beysens. Cluster formation in a granular medium fluidized by vibrations in low gravity. *Physical review letters*, 83(2):440–443, 1999.

[19] A. Fingerle and S. Herminghaus. Unclustering transition in freely cooling wet granular matter. *Physical review letters*, 97(7):78001, 2006.

[20] A. Fingerle and S. Herminghaus. Equation of state of wet granular matter. *Physical Review E*, 77(1):011306, 2008.

[21] A. Fingerle, K. Röller, K. Huang, and S. Herminghaus. Phase transitions far from equilibrium in wet granular matter. *New Journal of Physics*, 10(5):053020, 2008.

[22] I. Goldhirsch and G. Zanetti. Clustering instability in dissipative gases. *Physical review letters*, 70(11):1619–1622, 1993.

[23] PK Haff. Grain flow as a fluid-mechanical phenomenon. *Journal of Fluid Mechanics*, 134:401–30, 1983.

[24] O. Herbst, P. Müller, M. Otto, and A. Zippelius. Local equation of state and velocity distributions of a driven granular gas. *Physical Review E*, 70(5):051313, 2004.

[25] S. Herminghaus. Dynamics of wet granular matter. *Advances in Physics*, 54 (3):221–261, 2005. doi: 10.1080/00018730500167855.

[26] H. Hertz. Über die Berührung fester elastischer Körper. *Journal für die reine und angewandte Mathematik*, 92(156-171):22, 1882.

[27] D. J. Hornbaker, R. Albert, I. Albert, A. L. Barabási, and P. Schiffer. What keeps sandcastles standing? *Nature*, 387(6635):765–765, 1997.

[28] K. Huang, K. Röller, and S. Herminghaus. Universal and non-universal aspects of wet granular matter under vertical vibrations. *The European Physical Journal - Special Topics*, 179:25–32, 2009. ISSN 1951-6355. 10.1140/epjst/e2010-01191-5.

[29] M. M. Kohonen, D. Geromichalos, M. Scheel, C. Schier, and S. Herminghaus. On capillary bridges in wet granular materials. *Physica A: Statistical Mechanics and its Applications*, 339(1):7–15, 2004.

[30] I. M. Lifshitz and V. V. Slyozov. The kinetics of precipitation from supersaturated solid solutions. *Journal of Physics and Chemistry of Solids*, 19(1):35–50, 1961.

[31] C. C. Maaß, N. Isert, G. Maret, and C. M. Aegerter. Experimental investigation of the freely cooling granular gas. *Physical review letters*, 100(24):248001, 2008.

[32] F. Melo, P. B. Umbanhowar, and H. L. Swinney. Hexagons, kinks, and disorder in oscillated granular layers. *Physical review letters*, 75(21):3838–3841, 1995.

[33] M. E. Möbius, B. E. Lauderdale, S. R. Nagel, and H. M. Jaeger. Brazil-nut effect: Size separation of granular particles. *Nature*, 414:270, November 2001. doi: 10.1038/35104697.

[34] S. Nowak, A. Samadani, and A. Kudrolli. Maximum angle of stability of a wet granular pile. *Nature physics*, 1(1):50–52, 2005.

[35] J. S. Olafsen and J. S. Urbach. Clustering, order, and collapse in a driven granular monolayer. *Physical review letters*, 81(20):4369–4372, 1998.

[36] T. Pöschel and T. Schwager. *Computational Granular Dynamics: Models and Algorithms*. Springer, 2005. ISBN 9783540214854.

[37] Y. I. Rabinovich, M. S. Esayanur, and B. M. Moudgil. Capillary forces between two spheres with a fixed volume liquid bridge: theory and experiment. *Langmuir*, 21(24):10992–10997, 2005.

[38] S. H. E. Rahbari, J. Vollmer, S. Herminghaus, and M. Brinkmann. Fluidization of wet granulates under shear. *Physical Review E*, 82(6):061305, 2010.

[39] L. E. Reichl. *A Modern Course in Statistical Physics*. Physics Textbook. Wiley, 2009. ISBN 9783527407828.

[40] J. R. Royer, D. J. Evans, L. Oyarte, Q. Guo, E. Kapit, M. E. Mobius, S. R. Waitukaitis, and H. M. Jaeger. High-speed tracking of rupture and clustering in freely falling granular streams. *Nature*, 459(7250):1110–1113, June 2009. ISSN 0028-0836.

[41] K. Röller. *Numerical simulations of wet granular matter*. PhD thesis, Georg-August-Universität Göttingen, 2010.

[42] M. Scheel, R. Seemann, M. Brinkmann, M. Di Michiel, A. Sheppard, B. Breidenbach, and S. Herminghaus. Morphological clues to wet granular pile stability. *Nature materials*, 7(3):189–193, 2008.

[43] S. Strauch. Dynamical phase transitions of wet granular matter. Bachelor's thesis, Georg-August-Universität Göttingen, 2011.

[44] J. Trösemeier. Statistical Physics of Small Granular Systems with Hysteretic Interaction. Master's thesis, Georg-August-Universität Göttingen, 2012.

[45] S. Ulrich. *Aggregation and Gelation in Random Networks*. PhD thesis, Georg-August-Universität Göttingen, 2010.

[46] S. Ulrich, T. Aspelmeier, K. Röller, A. Fingerle, S. Herminghaus, and A. Zippelius. Cooling and Aggregation in Wet Granulates. *Phys. Rev. Lett.*, 102: 148002, Apr 2009. doi: 10.1103/PhysRevLett.102.148002.

[47] S. Ulrich, T. Aspelmeier, A. Zippelius, K. Röller, A. Fingerle, and S. Herminghaus. Dilute wet granular particles: Nonequilibrium dynamics and structure formation. *Physical Review E*, 80(3):031306, 2009.

[48] K. van der Weele, D. van der Meer, M. Versluis, and D. Lohse. Hysteretic clustering in granular gas. *EPL (Europhysics Letters)*, 53(3):328, 2001.

[49] C. D. Willett, M. J. Adams, S. A. Johnson, and J. P. K. Seville. Capillary bridges between two spherical bodies. *Langmuir*, 16(24):9396–9405, 2000.

[50] J. M. Yeomans. *Statistical Mechanics of Phase Transitions*. Oxford Science Publications. Oxford University Press, USA, 1992. ISBN 9780198517306.

[51] V. Y. Zaburdaev, M. Brinkmann, and S. Herminghaus. Free cooling of the one-dimensional wet granular gas. *Physical review letters*, 97(1):18001, 2006.

[52] T. Zhou. Effects of attractors on the dynamics of granular systems. *Physical review letters*, 80(17):3755–3758, 1998.

[53] H. P. Zhu and A. B. Yu. A theoretical analysis of the force models in discrete element method. *Powder technology*, 161(2):122–129, 2006.

[54] H. P. Zhu, Z. Y. Zhou, R. Y. Yang, and A. B. Yu. Discrete particle simulation of particulate systems: Theoretical developments. *Chemical Engineering Science*, 62(13):3378 – 3396, 2007. ISSN 0009-2509. doi: 10.1016/j.ces.2006.12.089.

Acknowledgements

First of all, I would like to express my gratitude to my supervisor Jürgen Vollmer for his dedication, steady enthusiasm and ongoing support, and both to him and Claus Heussinger for their commitment as a referee. Many thanks go to my family and fellow students for their ongoing support. Likewise, I want to acknowledge Claus Heussinger, Marco Mazza, Klaus Röller, and Jan-Hendrik Trösemeier for valuable and inspiring discussions, and Johannes Blaschke, Timo Graen, Jan-Hendrik Trösemeier, and Artur Wachtel for proof-reading. Last but not least I would like to thank the Department of Complex Fluids at the MPIDS and especially the Vollmer group for the great atmosphere, both scientific and personal.

Erklärung nach §18(8) der Prüfungsordnung für den Bachelor-Studiengang Physik und den Master-Studiengang Physik an der Universität Göttingen:

Hiermit erkläre ich, dass ich diese Abschlussarbeit selbständig verfasst habe, keine anderen als die angegebenen Quellen und Hilfsmittel benutzt habe und alle Stellen, die wörtlich oder sinngemäß aus veröffentlichten Schriften entnommen wurden, als solche kenntlich gemacht habe.
Darüberhinaus erkläre ich, dass diese Abschlussarbeit nicht, auch nicht auszugsweise, im Rahmen einer nichtbestandenen Prüfung an dieser oder einer anderen Hochschule eingereicht wurde.

Göttingen, den 31. August 2012

(Mitja Kleider)